Atom-by-atom Assembly of Individual Molecules

Adiabatically merging optical tweezers containing single atoms

Samuel J. M. White

Supervised by Prof Simon L. Cornish and Prof Simon A. Gardiner

Submitted in partial fulfilment of the requirements for the degree of
MSci in Natural Sciences (Chemistry, Mathematics and Physics)

April, 2021

Abstract

An important step in the construction of molecules from individual atoms is merging the optical tweezers containing the component atoms. In this report, we investigate how this can be completed in the shortest possible time while minimising atomic excitation and heating which would be detrimental to the association process. We focus on the case where a 938 nm optical tweezer containing a single ground state Cs atom is merged into a stationary 814 nm tweezer containing one ground state Rb atom. The relationship between the Cs effective potential minimum position and the location of the 938 nm tweezer is found and we use this to move this potential minimum with different trajectories. We find that using this procedure enables us to decrease the merging time by more than half whilst maintaining a $> 99\,\%$ combined probability that both atoms remain in their motional ground states. Furthermore, we explore new ways to complete the merge using a Lewis-Riesenfeld invariant-based inverse engineering method. This leads us to adjust the 938 nm tweezer beam power during the merge and move the Cs potential minimum with a specific trajectory which allows us to decrease the merge time by a further $20\,\%$. These techniques can be applied to other systems of optical tweezers utilising different atoms and will likely lead to similar improvements in the merging time.

Quantum Light and Matter
Department of Physics
Durham University

This work made use of the facilities of the Hamilton HPC Service of Durham University.

Contents

Introduction

The creation and trapping of ultracold molecules is of great interest in number of different areas of physics such as ultracold chemistry,[1–3] fundamental physics,[4,5] quantum computing[6] and quantum simulation.[7] This wide range of applications largely results from the additional properties molecules possess over their atomic counterparts such as vibrational and rotational degrees of freedom, anisotropic long-range interactions and, in the case of hetero-nuclear molecules, permanent dipole moments.[8,9]

Unfortunately, whilst the rich internal structure of molecules opens up many applications it makes cooling them using the traditional laser cooling techniques difficult.[10,11] An alternative to directly cooling high temperature molecules is to associate ultracold atoms using photoassociation or by utilising a Feshbach resonance.[1,12] After association, the resultant molecules can be transferred to their rovibrational ground state using a stimulated Raman adiabatic passage (STIRAP) procedure.[13–15]

Where individual molecules are to be created, highly focussed optical dipole traps (known as optical tweezers) are often used to confine single atoms.[1,16] The relatively high trap frequencies that can be achieved within these traps enables the application of Raman sideband cooling to cool atoms to their motional ground state.[17,18] This improves the efficiency of the magnetoassociation process between the atoms due to the large degree of wave function overlap.[19,20] Additionally, this provides a route for full quantum state control of the resultant molecule since no kinetic energy is produced during association processes utilising Feshbach resonances.[12]

Before association can occur, the separate optical tweezers containing the single atoms must be merged. This process has been demonstrated by Liu et al. for tweezers containing single Cs and Na atoms which were initially separated by 2.5 µm.[13] By using an adapted minimum jerk trajectory to complete the merging process in 7.6 ms, they experimentally achieved a 61(4) % combined probability that both atoms remain in their ground states after the merge.[13]

In this report we aim to establish methods which will allow this merging process to be completed faster whilst maintaining a high ground state probability for both atoms. Having the ability to complete fast adiabatic tweezer merging will become important when implementing arrays of optical tweezers containing ultracold molecules.[7] The construction of such arrays will require sequentially merging many pairs of tweezers,[21,22] thus minimising the individual merge times is important to reduce the impact of the finite lifetimes of the atoms when they occupy the same tweezer.

We will simulate the merging process between optical tweezers containing single Cs and Rb in their motion ground state. We will first cover the general background relevant to our investigation and outline the core features our simulations in chapters 1 and 2. In chapter 3, we simulate the motion of a single tweezer containing just the Cs atom in order to identify candidate trajectories for the merging process. We then consider methods to optimise the merging process in chapter 4. Finally, we present a summary of our findings and describe possible future research directions in chapter 5.

Chapter 1
Background

1.1 Optical dipole traps

In order to exert precise control over single atoms, they should first be individually trapped. For charged ions, trapping can be achieved utilising the Coulomb interaction, however it is clear that a different approach is required to trap neutral atoms.

It is possible to trap neutral atoms by utilising their interactions with laser radiation using optical dipole traps.[23] These traps are less dependent on the atomic state of the trapped atoms and can be used to create a greater number of different trapping geometries compared to the earlier magnetic traps.[24,25] Unfortunately, optical dipole traps have small trap depths ($\lesssim 1\,\mathrm{mK}$)[25] and are therefore usually loaded using magneto-optical traps (MOTs).[26] MOTs are commonly used as sources of cold and dense atomic gasses and utilise both magnetic fields as well as optical radiation to achieve simultaneous trapping and cooling.[16,25,27]

Recently, optical dipole traps have been constructed using highly focused Gaussian laser beams to form optical tweezers.[16,28] These permit the trapping of single atoms using the methods described in appendix C. Additionally, optical tweezers provide the environment necessary for the Raman sideband cooling of the atoms to their motional ground state (see appendix A).

For the purposes of our investigation, we will assume that single Cs and Rb have already been prepared in the motional ground state of two separate optical tweezers. In this section we will briefly outline some of the theory relating to optical dipole traps which is directly relevant to our investigation. We have considered the theory and methods relating to atomic cooling and trapping in some detail in appendices A to C.

1.1.1 The dipole force

The interaction between a radiation field and a neutral atoms can be equivalently viewed as either the result of a Lorentz force between the electromagnetic field and the induced dipole moment of the atom or in terms of momentum conservation from the absorption and emission processes of the atom in the field.[29] The components of this force can be split into two different types: the *scattering force* and the *dipole force*.[29] The scattering force results from the absorption of light by the atom and the subsequent spontaneous emission and is responsible for Doppler cooling (refer to section A.1).[30] In contrast, the dipole force results from the interaction between the induced atomic dipole moment and the optical field gradient and is related to stimulated emission processes.[31] Optical dipole traps, such as optical tweezers, utilise the dipole force to trap atoms.

A derivation illustrating how the dipole force arises from the induced-dipole interaction for a two-level atom in a radiation field is presented in appendix B. Alternatively, the interaction potential can be derived by modelling the atom as a simple harmonic oscillator

in a classical radiation field. The dipole force then arises from the resultant conservative potential as described by Grimm et al..[25] This treatment gives the interaction potential

$$U_{\text{dipole}}(\mathbf{r}) = -\frac{\alpha(\omega)}{2\epsilon_0 c} I(\mathbf{r}). \tag{1.1.1}$$

Here $I(\mathbf{r})$ is the intensity of the radiation field in the spatial coordinate $\mathbf{r}$ and $\alpha(\omega)$ is the real part of the complex, frequency dependent, ground state atomic polarisability with ω the frequency of the radiation field.

Real atoms have more than two energy levels, thus eq. (1.1.1) is not strictly valid and we should, in principle, use an expression dependent on the transition matrix elements for all possible transitions.[25] For ground state alkali atoms in red detuned traps, only the matrix elements related to the $ns \rightarrow np$ transitions, where n is the principle quantum number of the valence electron, contribute significantly. This permits the exclusive consideration of the transitions between the fine and hyperfine levels in the ns and np manifolds.

In many cases, the hyperfine splittings may be neglected since the frequency of the trapping light is sufficiently detuned from the atomic transition frequency that these splitting are not resolved.[25,32] We will further neglect the fine splitting and use eq. (1.1.1) since this produces sufficiently accurate results for our purposes.

1.1.2 Heating

The quantum nature of the scattering and dipole forces gives rise to force fluctuations which result in a heating effect.[29] In the scattering force, each absorbed photon is later emitted in a random direction via spontaneous emission and will cause the atom to recoil such that momentum is conserved, hence heating the atom.[33] This process is the origin of the Doppler cooling limit referred to in section A.1 of appendix A.

For the dipole force, the mean dipole force experienced by an atom is dependent on the populations of the combined atom-radiation field states (the dressed states) of the system. Transitions between the two different types of dressed state result in a reversal of the direction of the instantaneous dipole force experienced by the atoms causing heating.[34] The origin of this is explored in more detail in section B.2 within appendix B.

As we further discuss in section A.4, whilst we can counteract these heating processes using cooling methods when the atoms are in their individual optical tweezers, this is no longer possible after the tweezers have been merged. This leads to finite ground state lifetimes for the Cs and Rb atoms in the merged tweezer. Additionally, if at least one atom is not in the ground hyperfine state, then hyperfine-changing collisions may occur between the atoms releasing energy and leading to the loss of both atoms.[35,36] Although both atoms will be initially prepared in their lowest hyperfine states $(f_{\text{Cs}}, f_{\text{Rb}}) = (1, 3)$ where hyperfine-changing collisions are forbidden, the atoms may be transferred into states where hyperfine-changing collisions are possible via spontaneous Raman scattering.[35]

Whilst these processes occur on sufficiently long timescales that they have little effect when creating a single molecule, however the eventual aim of our experiment is to assemble a large number of molecules following a sequential merge process.[20] Minimising the tweezer

merging time will thus increase the probability that the atoms will still be in their ground state when the association process is completed, thus maximising the number of molecules which can be successfully created.

1.2 Fast adiabatic transport

Recently, there has been much interest in designing transport processes which are able to transport atoms at the highest possible speed maximal speed while maintaining a high transport fidelity.[37,38] This has a number of uses fields such as quantum information processing where systems may have a short coherence time[39,40] and has prompted research into finding the shortest possible route to transport an atom between two states.[38]

One of these techniques uses Lewis-Riesenfeld invariants to determine trajectories which allow adiabatic transport of atoms at short times. We will apply this method (described in section 1.2.1, below) to the merging of two optical tweezers for the first time. As discussed in section 1.1.2, the resultant shorter merging times should permit longer studies of molecules in optical tweezer arrays in the future.

1.2.1 Inverse engineering using Lewis-Riesenfeld invariants

In 1969, Lewis and Riesenfeld presented a method to use a Hermitian dynamical invariant $I(t)$ related to a known time-dependent Hamiltonian $H(t)$ by

$$\frac{\mathrm{d}I}{\mathrm{d}t} = \frac{\partial I}{\partial t} + \frac{i}{\hbar}[H, I] = 0, \tag{1.2.1}$$

to determine the eigenstates of the Hamiltonian in the far past and future where it is assumed constant.[41] This method can be reverse engineered to determine an appropriate time-dependent Hamiltonian which will result in a given state evolution.[37,42] This allows the determination of trajectories which permit fast, near adiabatic transport through the selection of appropriate initial and final states.

A one-dimensional, time-dependent Hamiltonian for a particle of mass m compatible with an invariant quadratic in momentum takes the form $H(t) = \frac{p(t)^2}{2m} + U(r,t)$ where[42,43]

$$U(r,t) = -F(t)r + \frac{1}{2}m\omega(t)^2 r^2 + \frac{1}{\rho(t)^2}V\left(\frac{r-\beta(t)}{\rho(t)}\right). \tag{1.2.2}$$

Here $F(t)$, $\omega(t)$, $\rho(t)$ and $\beta(t)$ are arbitrary functions satisfying

$$\ddot{\rho} + \omega(t)^2\rho = \frac{\omega_0}{\rho^3} \tag{1.2.3}$$

$$\text{and} \quad \ddot{\beta} + \omega(t)^2\beta = \frac{F(t)}{m}, \tag{1.2.4}$$

for ω_0 some constant which we set as $\omega_0 := \omega(0)$. The related dynamical invariant is given in this case by[42,43]

$$I = \frac{1}{2m}\left(\rho\left(p - m\dot{\beta}\right) - m\dot{\rho}(r-\beta)\right)^2 + \frac{1}{2}m\omega_0^2\left(\frac{r-\beta}{\rho}\right)^2 + V\left(\frac{r-\beta}{\rho}\right). \tag{1.2.5}$$

We may add an arbitrary purely time-dependent term to eq. (1.2.2), since this will produce no force and not affect the Physics of the situation.[42,44] Hence, setting $F(t) = m\omega(t)^2 r_0(t)$ and $V\left(\frac{r-\beta(t)}{\rho(t)}\right) = 0$ then adding the term $\frac{1}{2}m\omega(t)^2 r_0^2(t)$ to eq. (1.2.2) gives

$$U(r,t) = \frac{1}{2}m\omega(t)^2\big(r - r_0(t)\big)^2. \tag{1.2.6}$$

This is the potential term for a harmonic trap with angular frequency $\omega(t)$ with the centre of the trap given by $r_0(t)$. The constraint equation from eq. (1.2.4) then becomes Newton's second law of motion for a classical particle in a harmonic potential

$$\ddot{\beta} + \omega(t)^2\big(\beta - r_0(t)\big) = 0, \tag{1.2.7}$$

where we will identify the classical particle trajectory $r_c(t) = \beta(t)$. Using the Ehrenfest theorem, we can interpret $r_c(t)$ as the trajectory taken by the expectation value of the position for the transported particle. By rearrangement, we can write the location of the centre of the harmonic trap as

$$r_0(t) = \frac{\ddot{r}_c}{\omega(t)^2} + r_c, \tag{1.2.8}$$

and we can similarly rearrange eq. (1.2.3) for the angular frequency

$$\omega(t) = \sqrt{\frac{\omega_0^2}{\rho^4} - \frac{\ddot{\rho}}{\rho}}. \tag{1.2.9}$$

Considering the transport of a particle over a distance d in a time t_f where the final harmonic trap frequency $\omega(t_f) = \omega_0/\gamma$, we require

$$r_c(0) = 0, \quad r_c(t_f) = d \tag{1.2.10}$$

$$\text{and} \quad \rho(0) = 1, \quad \rho(t_f) = \gamma. \tag{1.2.11}$$

Additionally, it can be shown that demanding $\big[I(0), H(0)\big] = 0$ and $\big[I(t_f), H(t_f)\big] = 0$ such that the transport modes correspond with eigenfunctions of the Hamiltonian requires[42,44]

$$\dot{r}_c(0) = \dot{r}_c(t_f) = 0 \tag{1.2.12}$$

$$\dot{\rho}(0) = \dot{\rho}(t_f) = 0. \tag{1.2.13}$$

Similarly, satisfying eq. (1.2.1) requires[42,44]

$$\ddot{r}_c(0) = \ddot{r}_c(t_f) = 0 \tag{1.2.14}$$

$$\ddot{\rho}(0) = \ddot{\rho}(t_f) = 0. \tag{1.2.15}$$

An infinite number of functions $r_c(t)$, $\rho(t)$ can be found which satisfy these boundary conditions. In chapter 3 we consider some of these functions. It is important to note that when transport occurs in a rigid harmonic potential where $\omega(t) = \omega_0$, eqs. (1.2.11), (1.2.13) and (1.2.15) are all satisfied by $\rho(t) = 1$.

Chapter 2
Simulation construction

In this chapter we will outline the experimental data, methods and some of the fundamental theory that we have used to implement our simulations.

2.1 Optical Tweezers

2.1.1 Harmonic potential approximation

It is well-known that analytic functions can often be locally approximated around their critical points by quadratic functions. This allows us to approximate a wide range of potentials as harmonic close to their local minima and maxima.

In a number of places in this report, we will use that the potentials resultant from the optical tweezers (see section 2.1.2) can be modelled as harmonic potentials. In general, this is a reasonable approximation since the atoms being simulated usually remain in low energy states and are therefore only experience the effects of the potential in a small neighbourhood around the potential minimum. The anharmonic nature of the tweezer potentials becomes more important when we consider the effective potentials during the tweezer merging in chapter 4.

2.1.2 Trapping potential

The optical tweezers used to trap the single Rb and Cs atoms utilise a focussed Gaussian radiation beam as mentioned in section 1.1 and further explored in appendix C. For such a radiation beam, the spatial distribution of its intensity is given, in cylindrical coordinates (r, z), by[25,45]

$$I(r,z) = \frac{2P}{\pi w(z)^2} \exp\left(-\frac{2r^2}{w(z)^2}\right). \tag{2.1.1}$$

Here, P is the beam power, $w(z) := w_0\sqrt{1-\left(\frac{z}{z_R}\right)^2}$ where w_0 is the beam waist and the Rayleigh range $z_R := \pi\frac{w_0^2}{\lambda}$.

Using eq. (1.1.1), the resultant potential due to the dipole force interaction is

$$U(r,z) = -\frac{P\alpha}{\pi c\epsilon_0 w(z)^2} \exp\left(-\frac{2r^2}{w(z)^2}\right) = -U_0\frac{w_0^2}{w(z)^2} \exp\left(-\frac{2r^2}{w(z)^2}\right), \tag{2.1.2}$$

where $U_0 := \frac{P\alpha}{\pi c\epsilon_0 w_0^2}$ is the trap depth.

Considering one-dimensional slices of this potential along $z = 0$ and $r = 0$, the potentials

in the radial and axial directions are found to respectively be

$$U(r) = -U_0 \exp\left(-\frac{2r^2}{w_0^2}\right) \tag{2.1.3}$$

$$\text{and} \quad U(z) = -U_0 \frac{w_0^2}{w(z)^2} = -U_0 \left(1 - \left(\frac{z}{z_R}\right)^2\right)^{-1}. \tag{2.1.4}$$

In the case that the energy of the trapped atom is small in comparison to the potential depth ($k_b T \ll U_0$), the radial and axial potentials can be approximated by a cylindrically symmetric harmonic oscillator. The equation for this can be found by expanding eq. (2.1.3) and eq. (2.1.4) up to quadratic order and combining the resultant expressions to yield

$$U(r, z) = -U_0 \left(1 - \frac{2r^2}{w_0^2} - \frac{z^2}{z_R^2} + \mathcal{O}\left(r^4, z^4\right)\right). \tag{2.1.5}$$

Comparison of this equation in each dimension to the one-dimensional harmonic oscillator equation $U(x) = \frac{1}{2} m\omega^2 x^2$ permits the identification of harmonic trap frequencies in the radial and axial directions. These are found to be

$$\omega_r = \sqrt{\frac{4U_0}{m w_0^2}} \tag{2.1.6}$$

$$\text{and} \quad \omega_z = \sqrt{\frac{2U_0}{m z_R^2}}. \tag{2.1.7}$$

These harmonic trap frequencies are natural parameters to characterise the trapping potential and are used in the determination of the simulation units discussed in section 2.2.

In this work, we only simulate the radial component of the Gaussian potential given by eq. (2.1.3). Focussing on the radial component is justified since the trap is moved exclusively in the radial direction, thus the atom is much more likely to be excited in this coordinate.

Previous numerical simulations of merging tweezers containing Na and Cs atoms by Liu et al. found that when the radial and axial coordinates are considered independently, the probability of motional excitation was negligible in the axial direction compared to the radial direction.[13,45] Despite this, it may be possible that simulating a trap which simultaneously possesses a radial and axial coordinate could allow the identification of behaviour missed by completing separate simulations for each coordinate. This would also allow us to quantify the consequences of slight tweezer misalignments on the merging process. As such, a possible improvement to the current simulation would be for it to simulate a two-coordinate Gaussian potential.

For notional simplicity, we will now use ω instead of ω_r to refer to the harmonic trap frequency for a Gaussian potential in the radial coordinate.

2.1.3 Experimentally determined parameters

We have listed the experimental parameters used to construct the optical tweezer potentials we simulated in table 2.1. The real parts of the complex ground state atomic polarisabilities, $\alpha_{\mathrm{Cs}}(\lambda)$ and $\alpha_{\mathrm{Rb}}(\lambda)$, were calculated with the method described by Safronova et al. using the values they give for the required atomic parameters.[46]

λ (nm)	w_0 (µm)	P (mW)	$(\alpha_{\mathrm{Cs}}(\lambda), \alpha_{\mathrm{Rb}}(\lambda))$ $\left(\times 10^{-3}\ \mathrm{a}_0^3\right)$
814	0.92	1.38	$(-3.22, 4.76)$
938	1.06	3.13	$(2.89, 1.03)$

Table 2.1: The experimental parameters used for the optical tweezer potentials throughout this investigation.

The 814 nm optical tweezer will initially contain the Rb atom and the 938 nm tweezer will initially contain the Cs atom. The 814 nm tweezer is blue-detuned from the Cs D-line transitions (852 nm and 895 nm),[32] thus $\alpha_{\mathrm{Cs}}(814\,\mathrm{nm})$ is negative and the potential is repulsive for the Cs atom as shown in fig. 2.1(a).

For the Cs to remain trapped during the tweezer merge, we must have $\left|P_{814}\alpha_{\mathrm{Cs}}(814\,\mathrm{nm})\right| < \left|P_{938}\alpha_{\mathrm{Cs}}(938\,\mathrm{nm})\right|$ where P_{814} and P_{938} are the powers of the 814 nm and 938 nm tweezers respectively. Additionally, to prevent the Rb atom from spilling into the 938 nm tweezer and gaining excess energy during the merge we require $\left|P_{814}\alpha_{\mathrm{Rb}}(814\,\mathrm{nm})\right| > \left|P_{938}\alpha_{\mathrm{Rb}}(938\,\mathrm{nm})\right|$. Using wavelengths of 814 nm and 938 nm for the tweezers allows these conditions to be met whilst also minimising the scattering rates for both atoms, hence minimising their rate of heating via the photon scattering process discussed in section 1.1.2.[35]

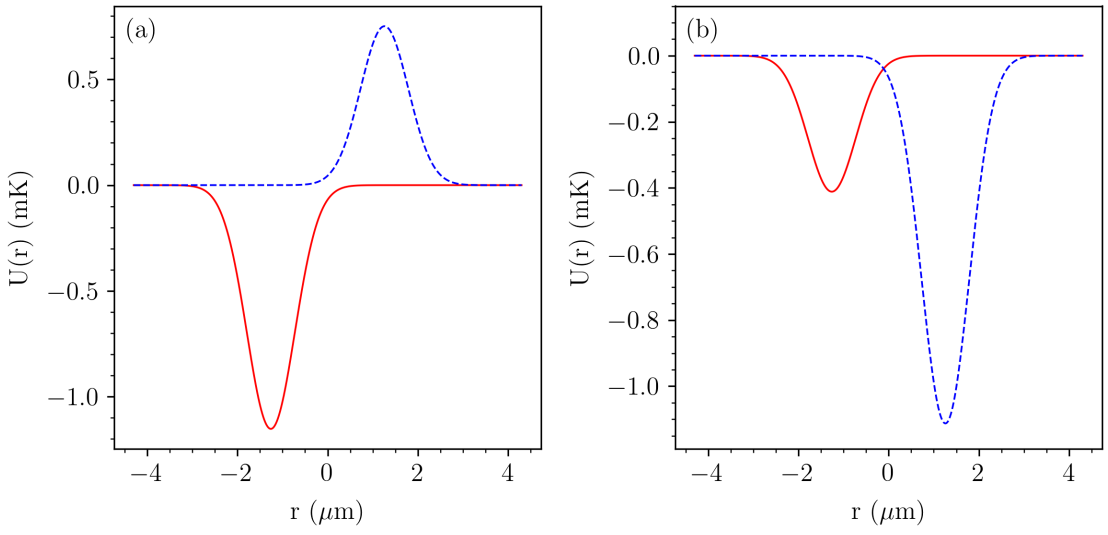

Figure 2.1: Optical tweezer potentials $U(r)$ used in our simulations (parameters are given in table 2.1) with their initial separation of 2.5 µm = 82 $\mathrm{a_h}$. In both figures, the solid red line gives the potential resultant from the 938 nm tweezer and the dashed blue line gives the potential from the 814 nm tweezer. (a) Potentials experienced by the Cs atom. (b) Potentials experienced by the Rb atom.

The tweezer powers used are equal to those used for loading the atoms into the optical

tweezers. As shown in fig. 2.1, these powers result in a trap depth of approximately 1.2 mK for each atom in its initial tweezer. Experimentally, the trap depths will be slightly shallower than this since we have not accounted for the imperfect transmission of the laser beams through the optical apparatus. In section 4.3 we will consider adjusting the tweezer powers during the merging process.

In the experimental apparatus, the beam waists were found to be radially asymmetric.[35] For our one-dimensional simulations, we have used the values measured for the beam waists along the merge coordinate.

In all of our merging simulations, we start with the optical tweezers separated by a distance of 2.5 µm (equivalent to 82 a_h, see section 2.2). This initial separation gives minimal overlap between the tweezer potentials for both atoms and hence ensures both atoms are initially in the isolated tweezer potentials. This can be seen by inspection of the tweezer potentials in fig. 2.1.

2.2 Units

The scales being modelled by the simulation are very small in comparison to those which SI units were designed to primarily describe. As such, a naïve implementation of SI units within the simulation would force the use of very small numbers which cannot be accurately manipulated using normal data types due to the constraints of floating point arithmetic.[47]

Whilst this issue could be mitigated by working with appropriate SI unit prefixes, we have instead defined a new unit system by setting three constants to be of unit value in the simulation. These constants were chosen to be

- the reduced Planck constant, $\hbar = 1.054\,572 \times 10^{-34}\,\mathrm{J\,s}$,[48]
- the mass of ^{133}Cs, $m_{\mathrm{Cs}} = 132.9055\,\mathrm{u} = 2.206\,947 \times 10^{-25}\,\mathrm{kg}$[48] and
- the radial harmonic trap frequency, $\omega = \sqrt{\frac{4U_0}{m_{\mathrm{Cs}} w_0^2}}\,\mathrm{s}^{-1}$ as given by eq. (2.1.6).

The choice of these allows certain key quantities to be expressed in a more natural way. For example, energy is expressed in units of $\hbar\omega$, thus the harmonic oscillator energy levels take half-integer values in these units. Additionally, these units allow the simplification of many calculations within the simulation by reducing the number of constants that need to be included. A description of how the SI base quantities are described in these simulation units is given in table 2.2.

Base quantity	Simulation unit	Symbol
Mass	m_{Cs}	
Time	$2\pi/\omega$	$\mathrm{T_h}$
Length	$\sqrt{\hbar/(m_{\mathrm{Cs}}\,\omega)}$	$\mathrm{a_h}$

Table 2.2: The simulation units associated with the SI base quantities. Base quantities not included within this table remain described by SI units within the simulation.

Throughout this report, we may refer to the time and length units listed in table 2.2 using the unit symbols we define in the table.

2.3 Numerical simulation methods

Within our simulations we used the split-step method (also known as the split operator method) to propagate our system in time.[49,50] We also used the split-step method to find the ground states of our system by propagating our system in imaginary time.[51]

Whilst developing our simulations, we evaluated the use of the short iterative Lanczos method for our time propagation.[49,50,52–54] We found that the split-step method offered better performance and stability for our one-dimensional simulations, however we expect that it may yield better performance for simulations involving multiple dimensions such as those mentioned in section 2.1.2. We discuss these simulation methods further in appendix D.

For the simulations in this report, we used a grid spacing of $\Delta r = 0.06\,\mathrm{a_h} = 1.8\,\mathrm{nm}$ on a grid of length $150\,\mathrm{a_h} = 4.6\,\mu\mathrm{m}$. In all simulations where the motional time was less than $15\,\mathrm{T_h} = 186\,\mu\mathrm{s}$ we used a timestep $\Delta t = 0.01\,\mathrm{T_h} = 0.12\,\mu\mathrm{s}$. In fig. 4.3, we used a slightly larger timestep of $\Delta t = 0.02\,\mathrm{T_h} = 0.25\,\mu\mathrm{s}$ for the simulations used to obtain results with motional times larger than $15\,\mathrm{T_h} = 186\,\mu\mathrm{s}$. This was required to reduce the time required to complete the simulations.

Chapter 3
One tweezer transport

We first simulated the motion of an isolated 938 nm tweezer containing a single Cs atom which was initially in its ground motional state. This allowed us to identify characteristics of the trajectories which are independent of the tweezer merging process.

In this chapter we will introduce the trajectories we used for the tweezer motion and present the results we obtained. All of our presented results relate to moving the single 938 nm tweezer a fixed distance $d = 82\,a_h = 2.5\,\mu m$, since this is the initial tweezer separation used in the merging process (see section 2.1.3). We vary the speed of the transport by changing the time the tweezer takes to move this fixed distance.

3.1 Linear trajectory

A linear trajectory involves transporting a particle constant speed with sharp accelerations at the start and end of the motion as shown in fig. 3.1(a). This is an example of a so-called 'bang-bang' trajectory, where there are abrupt changes in the acceleration during the motion.[37] This trajectory is worth considering due to the ease in which it can be implemented experimentally and the conceptual insight which it will allow into the behaviour observed when completing the transport with other trajectories.

3.1.1 Predictions for a harmonic potential

Using the results from section 1.2.1 on Lewis-Riesenfeld invariants, we will show that it is possible to satisfy the boundary conditions specified in eqs. (1.2.10), (1.2.12) and (1.2.14) when transporting an atom in a rigid harmonic potential using a linear trajectory. For a trajectory where these boundary conditions on the associated classical trajectory $r_c(t)$ are satisfied, we expect that there will be a high probability that the atom remains in its initial state after the transport is complete. Such a transport is said to be 'high-fidelity'. For this transport, the boundary conditions on $\rho(t)$ (eqs. (1.2.11), (1.2.13) and (1.2.15)) are trivially satisfied by $\rho(t) = 1$ due to the constant trap frequency.

We take the linear trajectory to be given by $r_0(t) = sd$. Here d is the transport distance and $s := t/t_f$ where t_f is the transport duration. Setting the trap frequency $\omega(t) = \omega_0$, we use eq. (1.2.8) to find

$$\ddot{r}_c + \omega_0^2 r_c = \omega_0^2 sd. \tag{3.1.1}$$

Solving this differential equation for r_c, we obtain

$$r_c(t) = A\exp(i\omega_0 t) + B\exp(-i\omega_0 t) + sd, \tag{3.1.2}$$

where A and B are constants that we will determine. Imposing the boundary conditions given by eqs. (1.2.10) and (1.2.12) yields

$$r_c(t) = -\frac{d}{t_f\omega_0}\sin(\omega_0 t) + d\frac{t}{t_f}, \quad \text{where} \quad t_f = \frac{2n\pi}{\omega_0} \quad \text{for} \quad n \in \mathbb{N}^* := \mathbb{N}\setminus\{0\}, \tag{3.1.3}$$

which automatically satisfies the boundary conditions given by eq. (1.2.14).

We can understand the restrictions on t_f by analysing the boundary conditions they come from and considering what they mean for a classical particle being moved in a harmonic potential. This analysis remains applicable in the quantum mechanical case when interpreted in the context of the position expectation value of the atomic wave function by the Ehrenfest theorem.

The $r_c(t_f) = d$ condition (eq. (1.2.10)) imposes that $t_f = \frac{n\pi}{\omega_0}$. This ensures that the particle is in the centre of the potential at the end of the transport and thus has minimal potential energy. The further restriction on t_f enforced by the $\dot{r}_c(t_f) = 0$ boundary condition (eq. (1.2.12)) requires that the particle has zero final kinetic energy due to the transport. Together these will minimise the energy gained by the atom during the transport process.

From these conditions, we expect that the transported particle might gain a maximal amount of excess energy during the transport if $t_f = \frac{(2n+1)\pi}{\omega_0}$. This is justified by noting that $\dot{r}_c(t_f)$ (and thus the kinetic energy) is maximal when this condition is met while the potential energy will be minimal.

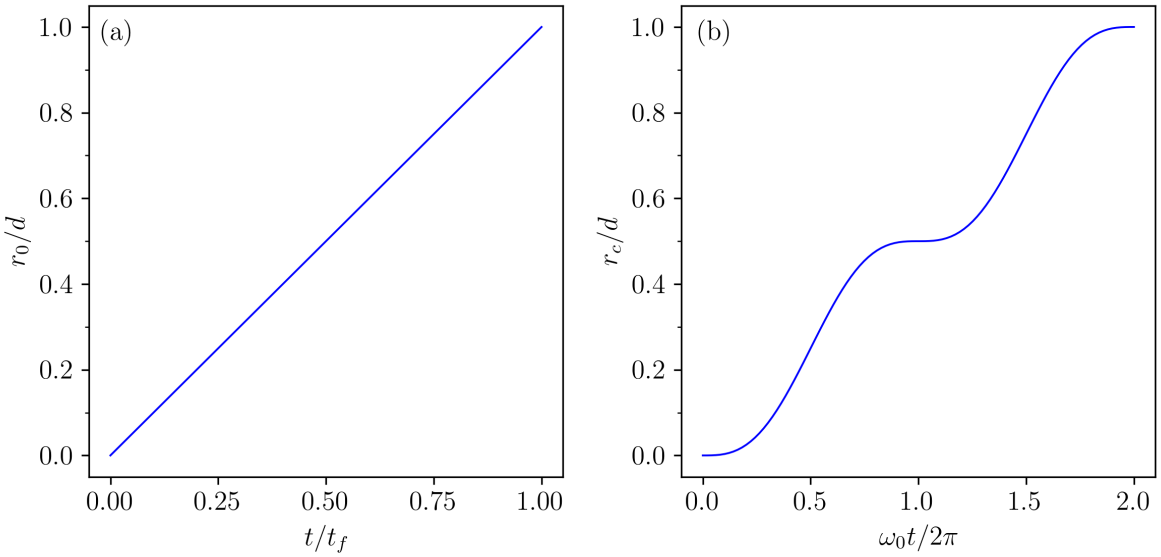

Figure 3.1: (a) The linear transport trajectory. Here r_0 is the position of the potential minimum, d is the total distance moved and t_f is the time taken for the transport. (b) The classical particle trajectory r_c during transport in a rigid harmonic trap with frequency ω_0 moving with a linear trajectory. We have plotted case where $t_f = 4\pi/\omega_0$ which is given by eq. (3.1.3) when $n = 2$.

We can gain a more intuitive understanding of this by by considering the energy transfers which occur during the transport of the classical particle. At the start of the transport, the potential is instantaneously displaced some fixed distance proportional to the transportation speed. Due to the harmonic nature of the potential, the potential energy gained by the particle will be equal to the kinetic energy associated with the motion of the potential. This results in the particle being stationary in the laboratory frame when it moves with maximal speed relative to the potential in the direction opposite to the transport direction. This is illustrated in fig. 3.1(b) where we have plotted the classical trajectory given by eq. (3.1.3) for the case of $n = 2$.

If the potential motion is stopped at the instant the particle is at rest in the laboratory frame and located in the centre of the potential, it will remain stationary and finish the transport in a low energy state. Similarly, if the atom has a maximal velocity at the centre of the potential when the transport concludes, it will instead be in a maximal energy state.

In section E.1 of appendix E, we have included URLs to animations which visually illustrate our discussions in this section.

3.1.2 Tweezer potential results

As explained in section 2.1.1, we expect that the Gaussian potential experienced by the Cs atom from the 938 nm optical tweezer will exhibit significant harmonic character and can be assumed to behave as a harmonic potential. We thus expect that the results found in section 3.1.1 will be valid for transporting the Cs atom in the 938 nm tweezer and we should observe faithful atomic transport when the transport time $t_f = n\mathrm{T_h}$ for $n \in \mathbb{N}^*$. Throughout this subsection, we will use that $n \in \mathbb{N}^*$.

Our results in fig. 3.2 show that this is partially true. For long transport times, where $t_f \gtrsim 10\,\mathrm{T_h}$, we see good agreement with the predictions of section 3.1.1. In this regime, the probability that the Cs atom was in the motional ground state after the transport P_{Cs}, was close to 100 % when $t_f = n\,\mathrm{T_h}$. As predicted, we also observe minima of P_{Cs} and maxima for the final Cs energy E_{Cs}, when $t_f = (n+1/2)\,\mathrm{T_h}$. As one might expect, we also found that the maxima of E_{Cs} decrease and the minima of P_{Cs} increase as the transport times are increased and the adiabatic transport regime is approached.

However, at short transport times the P_{Cs} maxima (and E_{Cs} minima) occur at longer transport times than expected. Additionally, The peak values for the P_{Cs} maxima are significantly less than one when $t_f \leq 3\,\mathrm{T_h}$. This behaviour is not reproduced when the simulations are repeated with a harmonic potential, thus we discount the possibility that they occur as a result of the simulation parameters we used or due to a numerical artefact. Instead, these effects result from the anharmonicity of the Gaussian potential. This anharmonicity reduces the effective trap frequency, thus leading to the longer oscillation period we observe.

This is reasonable since we expect that the effect of the Gaussian potential anharmonicity will more pronounced for shorter transport times, since the wave function has a greater energy during faster transports. This will result in the wave function experiencing the greater anharmonic character of the Gaussian potential further from the bottom of the potential.

Although we were able to achieve relatively high values of P_{Cs} for certain small values of t_f, it is unlikely that these will be achievable experimentally. In fig. 3.2, it is very clear that any small deviation in t_f from the values were the P_{Cs} maxima occur will result in large motional excitations for the Cs atom. This is especially pronounced for the shorter transport times. Experimentally, it will likely be difficult to ensure the tweezer control is sufficiently accurate and precise enough to precisely achieve the short transport times which give a fast and high-fidelity transport.

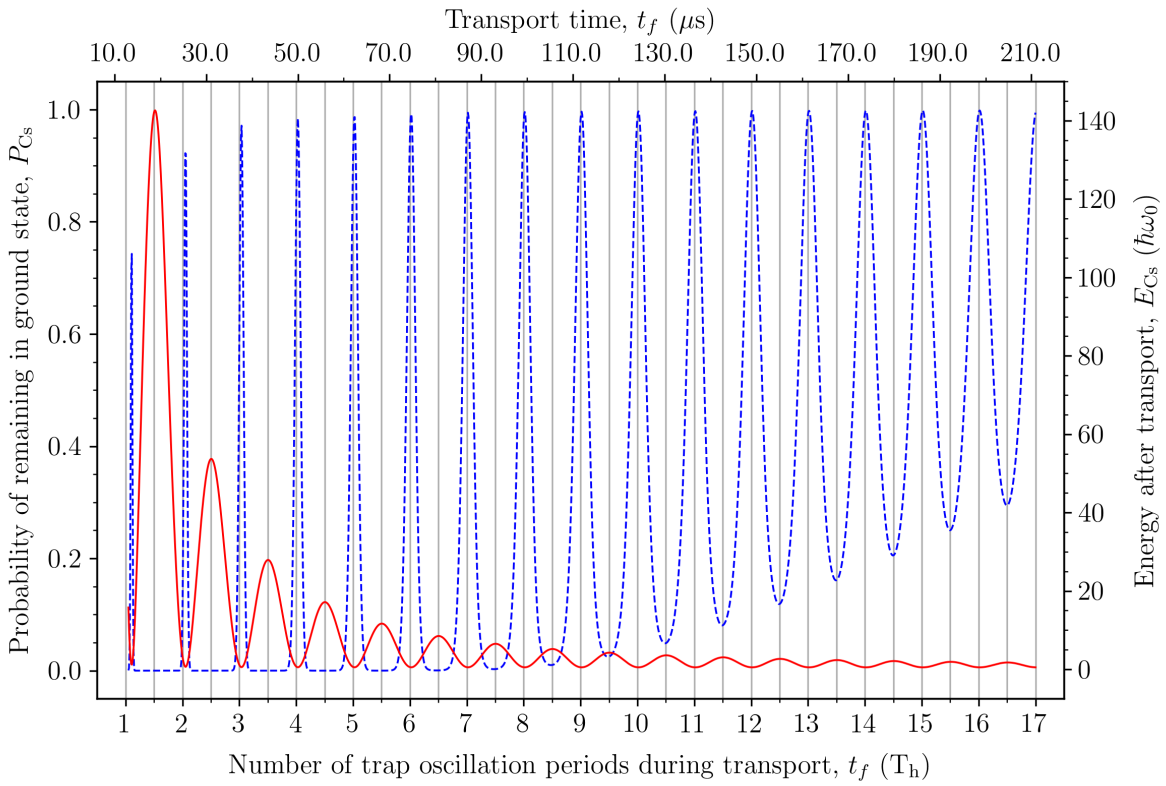

Figure 3.2: Results from transporting a Cs atom in the 938 nm tweezer using a constant speed, linear trajectory. The probability that the Cs atom remained in its ground state after the transport P_{Cs} is given by the dashed blue line and the final energy of the atom E_{Cs} is given by the solid red line.

3.2 Minimum-jerk trajectory

Liu et al. have previously merged optical tweezers containing single Cs and Na atoms using the so-called 'minimum-jerk trajectory' which is designed to transport the equilibrium point of a classical harmonic oscillator with minimal motional excitation.[13,45] This trajectory takes the functional form

$$r(t) = d\big(10s^3 - 15s^4 + 6s^5\big), \tag{3.2.1}$$

where d is the total distance moved, $s := t/t_f$ and t_f is the time over which the transportation takes place. This function is plotted in fig. 3.3(ii).

One of the aims of our investigation is to determine if a tweezer trajectory different to the minimum-jerk trajectory will allow a faster tweezer merging. As such, this trajectory acts like a control for us to benchmark our methods against.

By using the minimum-jerk trajectory plotted in fig. 3.3(ii) to control the position of the 938 nm optical tweezer, we obtain the results in fig. 3.3(i). Immediately, it is clear that the Cs ground state occupation probability following transport P_{Cs} reaches consistently high values at much shorter transport times than we saw for the linear trajectory in fig. 3.2.

For small values for the transport time t_f, the P_{Cs} maxima and minima show a clear periodic dependence on t_f similar to that seen for the linear trajectory. This occurs since

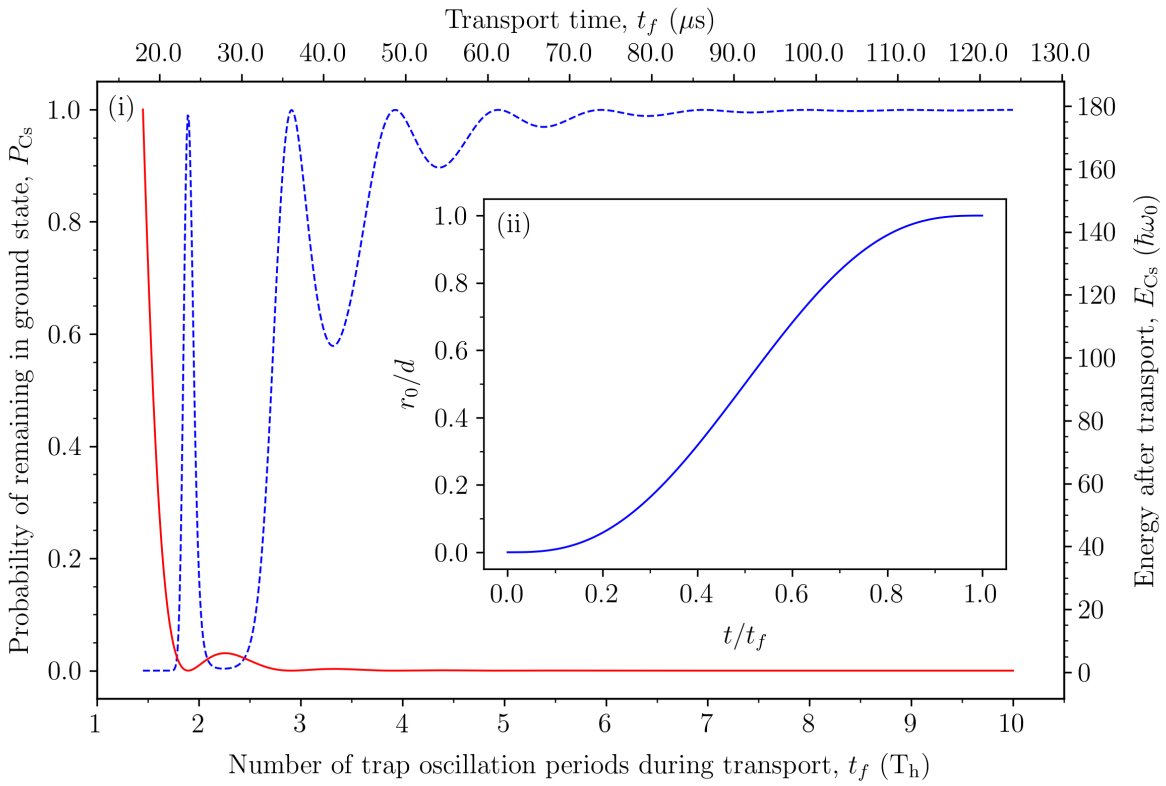

Figure 3.3: (i) Results from transporting a Cs atom in the 938 nm tweezer using the minimum-jerk trajectory. The probability that the Cs atom remained in its ground state after the transport P_{Cs} is shown by the dashed blue line while the final energy of the atom E_{Cs} is given by the solid red line. (ii) The minimum-jerk trajectory where $r_0(t)$ is the tweezer position, d is the transport distance and t_f is the total time taken for the transport.

the Cs position expectation value starts oscillating in the potential during the transport in a similar manner to that seen for the linear transport. Due to this motional excitation, the exact transport duration becomes important in order to satisfy the $r_0(t_f) = d$ and $\dot{r}_0(t_f) = 0$ boundary conditions.

The smooth acceleration of the minimum-jerk trajectory results in a smaller motional excitation during transport than if a linear trajectory is used, thus the P_{Cs} minima occur at much higher values than those in fig. 3.2. This periodic behaviour of P_{Cs} continues as the value of t_f increases, however the amplitude of these probability oscillations continue to decrease as the adiabatic regime is approached. We obtain $P_{Cs} > 99\,\%$ for all transports with $t_f > 6.54\,T_h = 81.1\,\mu s$ (refer to table F.1 of appendix F for more details).

Unsurprisingly, this trajectory yields overall better results than those seen for the linear trajectory as we are able to obtain high fidelity transport at much lower values of t_f without requiring highly precise and accurate control over the tweezer motion.

3.3 Lewis-Riesenfeld trajectories

As stated in section 1.2.1, an infinite number of classical trajectories $r_c(t)$ can be found which satisfy the boundary conditions given by eqs. (1.2.10), (1.2.12) and (1.2.14). In this section, we only consider a single example of $r_c(t)$ resultant from assuming that it takes

the form of a fifth order polynomial. The use of other functions for $r_c(t)$, such as the Fourier series form studied by Lam et al.,[38] may yield better results and are a potentially interesting direction for further exploration of the problem.

3.3.1 Polynomial ansatz

As introduced above, by using the fifth order polynomial ansatzes of $r_c(t) = \sum_{i=0}^{5} \beta_i s^i$ and $\rho(t) = \sum_{i=0}^{5} \rho_i s^i$ where $s := t/t_f$, we can satisfy the boundary conditions given by eqs. (1.2.10), (1.2.12) and (1.2.14) if we take[42,44]

$$r_c(t) = d\big(10s^3 - 15s^4 + 6s^5\big) \tag{3.3.1}$$

$$\text{and} \quad \rho(t) = 1 + 10(\gamma - 1)s^3 - 15(\gamma - 1)s^4 + 6(\gamma - 1)s^5. \tag{3.3.2}$$

Notice that the function for $r_c(t)$ we find is the minimum-jerk trajectory given in eq. (3.2.1). This is not unexpected, since the minimum-jerk trajectory is the optimum classical trajectory (see section 3.2) and $r_c(t)$ is the classical solution to the harmonic oscillator equation eq. (1.2.8).

Using eq. (1.2.8) with $r_c(t)$ given by eq. (3.3.1) we obtain

$$r_0(t) = d\frac{60s - 180s^2 + 120s^3}{\big(t_f\omega(t)\big)^2} + r_c(t). \tag{3.3.3}$$

Since $r_0(t)$ depends on the total transport time t_f, it represents a class of trajectories. In this report we will refer to the trajectories we have found using this fifth order polynomial ansatz as the Lewis-Riesenfeld trajectories.

Considering the limit of large transportation times $t_f \to \infty$ and assuming that $\omega(t)$ is bounded, we have $1/t_f\omega(t) \to 0$ so $r_0(t) \to r_c(t)$. Thus demonstrating that the minimum-jerk trajectory is the classical limit of the Lewis-Riesenfeld trajectories as we expect from the correspondence principle.

By substituting $\rho(t)$ from eq. (3.3.2) into eq. (1.2.9), we may similarly obtain an expression for the angular frequency of the harmonic trap. We will consider this more in section 4.3.

3.3.2 Application to single tweezer transport

Using the trajectories given by eq. (3.3.3) and setting $\omega(t) = \omega_0$ in our single tweezer transport simulation, we obtain the results shown in fig. 3.4(i). As we have discussed, the tweezer trajectories are different for different values of the transportation time t_f. This is shown in fig. 3.4(ii), where we have plotted the trajectories for three different values of t_f (blue, red and green lines) and can see how the trajectories converge to the minimum-jerk trajectory (black dotted line) as t_f increases.

In fig. 3.4(i), we see that the probability of the Cs atoms being in the ground state after the transport P_{Cs} rapidly increases when $t_f > 1.2\,\mathrm{T_h}$ and we obtain $P_{\mathrm{Cs}} > 99\,\%$ for all transports taking longer than $1.67\,\mathrm{T_h} = 20.7\,\mu\mathrm{s}$. We do not observe the probability fluctuations seen for the linear and minimum jerk trajectories since the wave function is not motionally excited within the potential during transport in the same way. During a

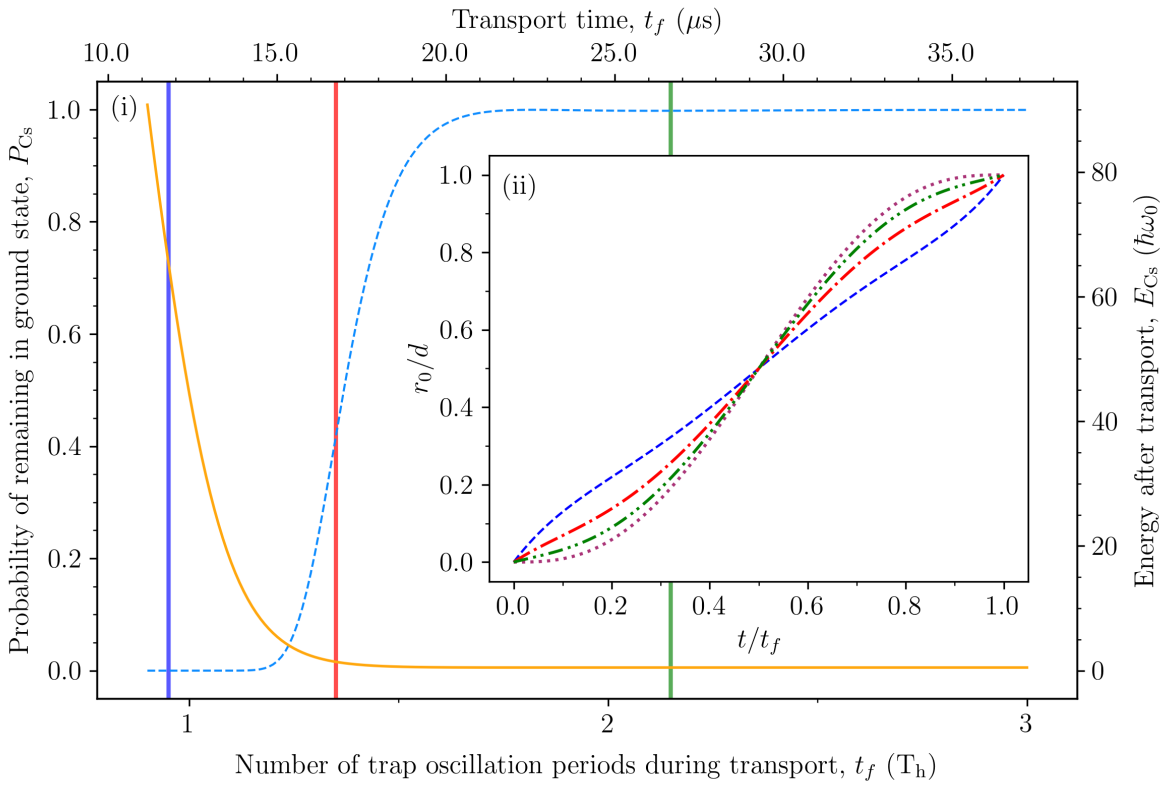

Figure 3.4: (i) Results from moving the 938 nm tweezer using the Lewis-Riesenfeld trajectories given by eq. (3.3.3). The probability that the atom remained in its ground state after the transport P_{Cs} is given by the dashed pale blue line and the final energy of the Cs atom E_{Cs} is given by the solid orange line. The three coloured vertical lines correspond to the transport times t_f for the trajectories shown in the (ii). (ii) An illustrative sample of the Lewis-Riesenfeld trajectories used. Here, $r_0(t)$ is the optical tweezer position, d is the distance the Cs transported and t_f is the total transport time. The dashed blue line gives the trajectory for $t_f = 0.95\,T_h$ (blue vertical line in (i)), the dash-dotted red line shows the trajectory for $t_f = 1.35\,T_h$ (red line in (i)) and the dash-double-dotted green line gives the same for $t_f = 2.15\,T_h$ (green line in (i)). The dotted purple line shows the minimum-jerk trajectory which is the limit of the Lewis-Riesenfeld trajectories as $t_f\omega_0 \to \infty$.

transport with a Lewis-Riesenfeld trajectory, the wave function is driven up one side of the potential during the first half of the motion, before the process is mirrored in reverse for the final half. This is shown in the animations in section E.4 of appendix E.

The values for P_{Cs} obtained when $t_f < 1.2\,T_h$ are found to be due to the anharmonicity of the Gaussian potential. With a perfectly harmonic potential, we found that it is possible to maintain high ground state probabilities when $t_f < 0.5\,T_h$.

The effects of the anharmonicity of the tweezer potential, could potentially be reduced by increasing the power of the trapping radiation and thus making the tweezer potential deeper. However, doing this does not have such a straightforward effect on the merging process since it will also effect the probability that the Rb atom in the 814 nm tweezer becomes motionally excited. We will discuss altering the tweezer beam powers (and thus the potential depths) in section 4.3.

Chapter 4
Merging two tweezers

We will now turn our attention to the merging process between the two tweezers. In this process, both tweezers initially contain single atoms in their ground motional state and the 938 nm tweezer (containing the Cs atom) is moved whilst the 814 nm tweezer (containing the Rb atom) is held in a fixed position.

We have not modelled the interactions between the atoms since we assume that we will be able to find an appropriate Feshbach resonance such that the Cs and Rb interspecies interactions can be tuned to zero. In the future, it may be interesting to consider the effects of non-zero interatomic interactions on the merging process.

4.1 Effective potential considerations

When merging the two optical tweezers, the effective potential experienced by each atom is the linear sum of the potentials experienced by the atom from each optical tweezer. Using eq. (2.1.3), this is given by

$$U(r,t) = -U_{814}\exp\left(-\frac{2(r-r_{814})^2}{w_{814}^2}\right) - U_{938}\exp\left(-\frac{2\big(r-r_{938}(t)\big)^2}{w_{938}^2}\right), \tag{4.1.1}$$

where U_{814}, U_{938} are the trap depths; w_{814}, w_{938} are the beam waists and r_{814}, $r_{938}(t)$ are the locations of the 814 nm and 938 nm tweezers respectively.

Due to our choice of trap frequencies and powers, the effective potential in the neighbourhood of each atom consists of a single potential minimum (see section 2.1.3). This allows us to continue utilising the harmonic approximation for our potentials, however the merging process introduces additional complexities to this approximation which were not present in the single tweezer transport. In this section we will identify these complexities and will start exploring ways in which we can compensate for their effects.

4.1.1 Trajectory compensation

During the tweezer merging process, there is no longer a direct correspondence between the tweezer positions and the locations of the potential minima experienced by each atom. This can be seen in fig. 4.1(a) where the position of the effective potential minimum for the Cs atom (solid blue line) deviates from the 938 nm tweezer position (dashed red line) as it is moved with a linear trajectory. This deviation begins as the potentials due to each tweezer start to merge at $t/t_f \approx 0.4$ where t_f is the total time for the merge. At $t = t_f$, the tweezers are fully merged and the centres of the tweezer potentials are aligned, so this deviation disappears.

The effective potential experienced by the Cs atom $U_{\mathrm{Cs}}(r,t)$ can be found by using appropriate values for U_{814} and U_{938} in eq. (4.1.1). By solving $\frac{\partial U_{\mathrm{Cs}}(r,t)}{\partial r}|_{r_{\min}(t)} = 0$ where $r_{\min}(t)$ is the location of the Cs atom potential minimum, we can find the 938 nm tweezer position r_{938} as a function of $r_{\min}$. This thus allows us to determine how we should move the 938 nm

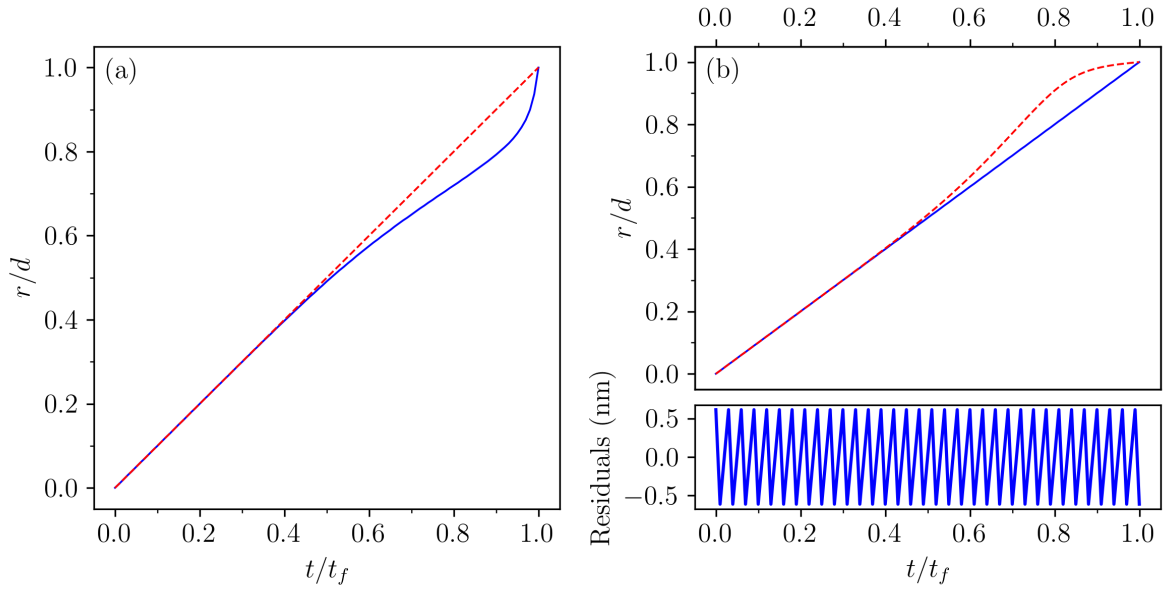

Figure 4.1: The 938 nm optical tweezer and Cs potential minimum positions during a tweezer merging processes taking a time t_f where the tweezers are initially separated by a distance $d = 2.5\,\mu\text{m}$. The solid blue lines give the potential minimum location and the dashed red lines show the 938 nm tweezer position. (a) Moving the 938 nm with a linear trajectory results in the Cs potential minimum moving with a non-linear trajectory due to the effects of the merging potentials. (b) By moving the 938 nm optical tweezer with a trajectory calculated using eq. (4.1.2), the Cs potential minimum is made to move with a linear trajectory. The residuals shown are those between the Cs potential minimum location and a linear trajectory and have a magnitude smaller than half the spatial grid spacing $\Delta x/2 = 0.9\,\text{nm} = 0.03\,a_\text{h}$.

optical tweezer such that the potential minimum moves with our desired trajectory. Completing this process yields

$$\begin{aligned} r_{938}(t) &= r_\text{min} \pm \frac{1}{2} w_{938} \sqrt{-W(-A^2)} \\ \text{where} \quad A &:= \frac{2U_{814}\, w_{938}}{U_{938}\, w_{814}^2} (r_\text{min} - r_{814}) \exp\left(-\frac{2(r_\text{min} - r_{814})^2}{w_{814}^2} \right). \end{aligned} \tag{4.1.2}$$

In this equation, $W(z)$ is the Lambert W-function which is defined to be the function satisfying[55,56]

$$W(z) \exp\big(W(z)\big) = z \quad \text{for} \quad z \in \mathbb{C}. \tag{4.1.3}$$

Unfortunately, $W(z)$ cannot be expressed in terms of elementary functions. Additionally, the values for $-A^2$ which are relevant for our experiment lie within the interval $(-1/e, 0)$ for which $W(-A^2)$ is double valued.[56] Using the Lagrange inversion theorem, we can find a series expansion for the principle branch $W_0(z)$ about $z = 0$ given by[56,57]

$$W_0(z) = \sum_{n=1}^{\infty} \frac{(-n)^{n-1}}{n!} z^n \quad \text{for} \quad |z| < \frac{1}{e}. \tag{4.1.4}$$

From inspection of fig. 4.1(a), it is clear that only the positive square root value in eq. (4.1.2) is relevant for correcting the 938 nm tweezer position. We have found that using this with the tenth order series expansion of $W_0(-A^2)$ yields sufficiently accurate results as shown in fig. 4.1(b).

In fig. 4.1(b), we see that the maximum values for the residuals between the Cs potential minimum location and a linear trajectory are less than half the spatial grid size $\Delta x/2 = 0.03\,\mathrm{a_h} = 0.9\,\mathrm{nm}$ (refer to section 2.3). This and the uniformly periodic nature of the residuals throughout the merging process indicate that these errors result from our finite spatial grid spacing instead of from errors in the trajectory compensation. We similarly find that the deviations between the Cs potential minimum location and its intended location remain less than $\Delta x/2$ for all of the other trajectories we have tested.

We also observe that the effective potential global minimum for the Rb atom moves during the merging process despite the 814 nm tweezer being kept in a fixed position. For short merge times, this results in some motional excitation of the Rb atom, however for all of the trajectories except those in section 4.3 that we consider, this excitation is much less than that experienced by the Cs atom. This can be seen in table F.2 of appendix F.

4.1.2 Harmonic trap frequencies

During the tweezer merging process, the harmonic trap frequencies experienced each atom will change. Using a similar method to that described in section 2.1.2, we Taylor expand the effective potential given by eq. (4.1.1) up to quadratic order about the relevant optical tweezer location a. Comparing the resultant quadratic terms to $\frac{1}{2}m\omega_a^2 a^2$ gives the harmonic trap frequency

$$\omega_a^2 = \frac{4}{m}\left(\frac{U_a}{w_a^2} - \frac{U_b}{w_b^2}\left(\frac{4(a-b)^2}{w_b^2} - 1\right)\exp\left(-\frac{2(a-b)^2}{w_b^2}\right)\right). \tag{4.1.5}$$

Here, U_a is the trap depth and w_a is the beam waist for the optical tweezer with position given by a. Similarly, b, U_b and w_b are the position, trap depth and beam waist respectively for the other tweezer. This equation remains valid as long as the tweezer location a remains close to the position of the minimum in the effective potential. In this case, the difference between these two positions will only introduce linear terms in the Taylor expansion so the quadratic terms (and hence ω_a) will be unaffected. We will assume that this is true in our simulations, however if the trajectory compensation given by eq. (4.1.2) becomes too large this may no longer hold, thus introducing an error in our value of ω_a.

As we expect, we recover the result given in eq. (2.1.6) for the harmonic frequency of an isolated Gaussian potential when we take the limit of an infinitely large tweezer separation $(a-b) \to \infty$ in eq. (4.1.5). We also see that when $a - b = w_b/2$, the difference between ω_a and its limiting value at infinite tweezer separation changes sign. This occurs when a coincides with position of the inflection point for the Gaussian potential resultant from the tweezer at b.

In fig. 4.2, we have plotted how the harmonic trap frequencies change during the merging of the 938 nm and 814 nm optical tweezers using eq. (4.1.5). For Cs (solid red line), the trap frequency initially increases as the repulsive potential resultant from the 814 nm tweezer is approached and causes the Cs effective potential to constrict. The trap frequency then falls as the shallower effective potential depth takes effect. From the perspective of the Rb atom (dashed blue line), the opposite occurs and the trap frequency initially falls as the

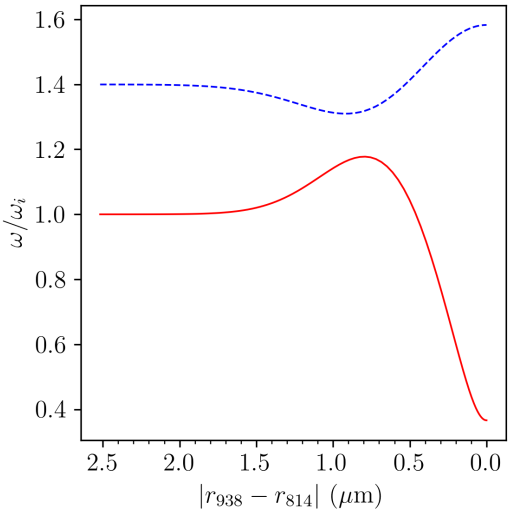

Figure 4.2: Harmonic trap frequencies ω experienced by the Cs atom (solid red line) and Rb atom (dashed blue line) during the tweezer merging process. These are presented as a function of the optical tweezer separation $|r_{938} - r_{814}|$ and are plotted relative to the initial trap frequency experienced by the Cs atom ω_i.

Rb effective potential becomes wider due to the merging of the two attractive potentials. This later reverses as the trap depth of the effective potential increases.

Due to these changes in the trap frequency, we will report the post-merge atomic energies using the harmonic trap frequency for each atom after the merge ω_f. Additionally, from now we will only refer to the merging times using SI units.

4.2 Minimum-jerk and Lewis-Riesenfeld trajectories

In this section, we present results obtained by merging the optical tweezers were the 938 nm tweezer is moved using eq. (4.1.2) such that the Cs potential minimum moves with our specified trajectory. We consider the minimum-jerk trajectory and two classes of Lewis-Riesenfeld trajectories; rigid Lewis-Riesenfeld trajectories identical to those used in section 3.3 and non-rigid Lewis-Riesenfeld trajectories where we calculate the harmonic trap frequency at each timestep using eq. (4.1.5) and use this in the trajectory calculation (see eq. (3.3.3)). Our results are shown in fig. 4.3.

In our results, we reach high ground state occupation probabilities for the Cs atom P_{Cs} for all of the trajectories at significantly longer merge times t_f than those found for the one-tweezer transport in chapter 3. This is primarily attributed to the changes in the Cs harmonic trap frequency during the merging process which we will explore in section 4.3. We have not plotted any data for the Rb atom here since its ground state occupation probability P_{Rb} is much higher P_{Cs} for all values of t_f (we show this in table F.2 of appendix F).

The minimum-jerk trajectory (dashed lines), exhibits behaviour similar to that seen in section 3.2 with the final Cs energies E_{Cs} and values of P_{Cs} showing a periodic dependence on t_f. This continues at longer merge times as shown in the inset, where the amplitudes of the probability oscillations decrease as t_f increases and the adiabatic regime is approached.

The rigid Lewis-Riesenfeld trajectories (solid lines) show a very small improvement over the minimum-jerk trajectory and the non-rigid Lewis-Riesenfeld trajectories (dot-dashed

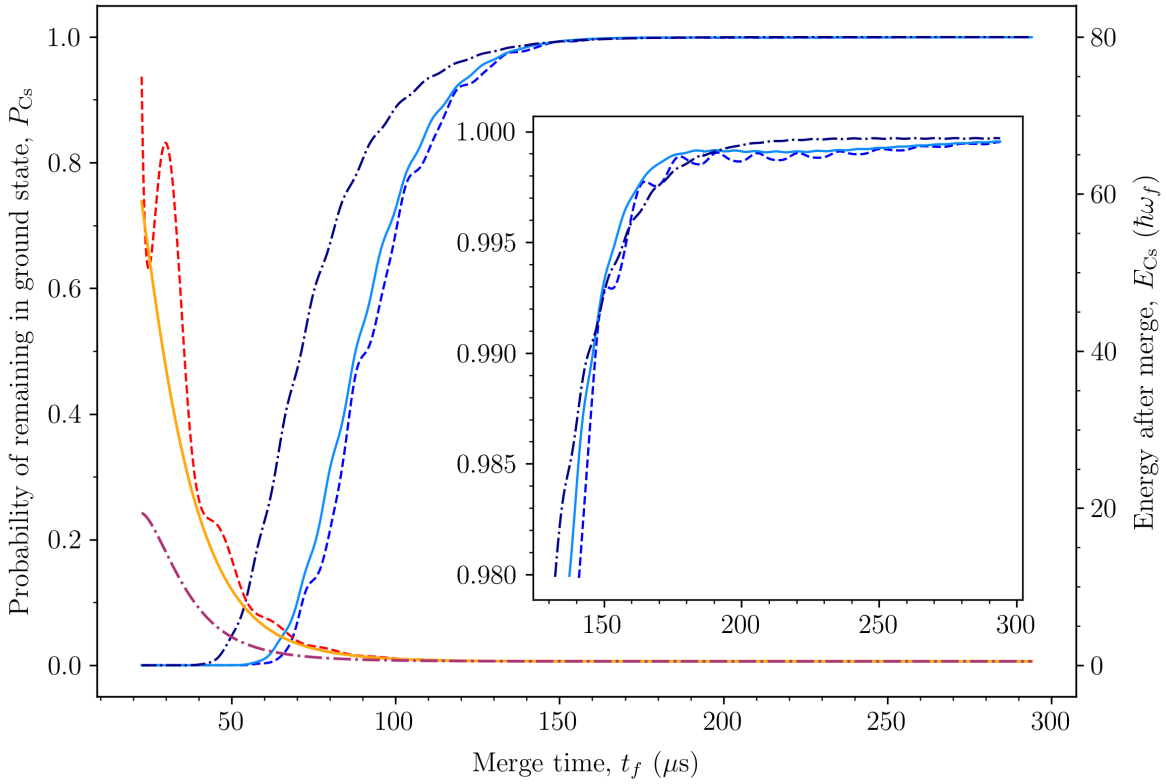

Figure 4.3: The probability that the Cs atom remains in its motional ground state P_{Cs} (blue and navy lines, increasing with t_f) and its energy after the merge E_{Cs} (red, orange and purple lines, decreasing with t_f), when merging the two optical tweezers. The 938 nm tweezer is moved such that the effective potential minimum for the Cs atom follows a minimum jerk (dashed lines), rigid Lewis-Riesenfeld (solid lines) or non-rigid Lewis-Riesenfeld (dot-dashed lines) trajectory, by using eq. (4.1.2). We compute the rigid Lewis-Riesenfeld trajectories using the harmonic trap frequency for a Cs atom in the 938 nm tweezer Gaussian potential. The non-rigid Lewis-Riesenfeld trajectories are instead computed using the trap frequencies found using eq. (4.1.5) at each timestep. The energies in the main figure are plotted relative to harmonic frequency of the Cs effective potential at the end of the merge ω_f. The inset shows the detailed behaviour of P_{Cs} when $P_{Cs} > 98\,\%$. The small discontinuities seen in the inset at $t_f = 186\,\mu s$ result from a change in the simulation timestep from 0.12 µs (for $t_f \leq 186\,\mu s$) to 0.25 µs (for $t_f > 186\,\mu s$) and does not represent physical behaviour.

lines) show a further moderate improvement when $t_f \lesssim 140\,\mu s$. Both classes of Lewis-Riesenfeld trajectories yield values for P_{Cs} which weakly oscillate with t_f, although this is much less pronounced than in the minimum-jerk trajectory. This indicates that both are unable to prevent significant motional excitations of the Cs atom during the merging process.

In the inset of fig. 4.3, we see that all three types of trajectory exceed $P_{Cs} = 99\,\%$ for $t_f \approx 150\,\mu s$. The combined ground state occupation probabilities for both the Cs and Rb atom $P_{combined} = P_{Cs} \times P_{Rb}$ similarly exceed 99 % when $t_f \approx 150\,\mu s$ (shown in table F.2). In our experiment, we require that both atoms are in their ground state for successful molecule formation to occur,[19,20] thus require very high values for $P_{combined}$. Thus, when using this method the choice between these trajectories is fairly inconsequential.

When not using eq. (4.1.2) to correct the tweezer trajectory, we found that $t_f > 350\,\mu s$ is required to to achieve $P_{Cs} > P_{combined} > 99\,\%$ (refer to section G.1 and table F.3).

4.3 Trap frequency control

In the previous section, we stated that the main reason we achieved lower ground state probabilities than we found for the single tweezer motion in chapter 3, is that the Cs trap frequency changes during the merging process. So far in this report, we have only considered satisfying the Lewis-Riesenfeld boundary conditions on the Cs classical trajectory $r_c(t)$ (eqs. (1.2.10), (1.2.12) and (1.2.14)) which is related to potential minimum position by eq. (1.2.8). However, the inverse engineering method using Lewis-Riesenfeld invariants discussed in sections 1.2.1 and 3.3.1 also imposed boundary conditions on $\rho(t)$ (eqs. (1.2.11), (1.2.13) and (1.2.15)) which is related to the harmonic trap frequency by eq. (1.2.10). These boundary conditions are not satisfied with the merging procedure we used in section 4.2 due to the uncontrolled changes in the Cs atom trap frequency.

In principle, we can control the trap frequency for one of the atoms during the merging process by appropriately adjusting the beam power for one of the optical tweezers. By re-arranging eq. (4.1.5) we can find

$$U_a = w_a^2 \left(\frac{1}{4} m\omega_a^2 + \frac{U_b}{w_b^2} \left(\frac{4(a-b)^2}{w_b^2} - 1 \right) \exp\left(-\frac{2(a-b)^2}{w_b^2} \right) \right), \tag{4.3.1}$$

then using the trap depth definition from section 2.1.2 we relate U_a to the beam power

$$P_a = \frac{\pi c \epsilon_0 w_a^2}{\alpha} U_a.$$

In our simulations, we will treat eq. (4.3.1) as being independent of eq. (4.1.2) and will use the tweezer locations a and b from the previous simulation timestep to determine the tweezer power for the current timestep. This approximation results in the sub-optimal trap frequency control shown in fig. 4.4(ii).

By adjusting the power of the 938 nm tweezer during the merging process we can attempt to keep the Cs harmonic trap frequency fixed at its initial value. From the perspective of the Cs atom, this should make the merging process similar to the single tweezer transport studied in chapter 3, where the Lewis-Riesenfeld boundary conditions on $\rho(t)$ are trivially satisfied. Our results for this are presented in fig. 4.4.

In fig. 4.4(i), we see that the Cs ground state occupation probability P_{Cs} exceeds 99 % for merge times $t_f > 54.8\,\mu\mathrm{s}$. This is less than half the value of t_f required to achieve the same P_{Cs} in section 4.2, but is still significantly larger than the $t_f = 20.7\,\mu\mathrm{s}$ threshold found for the single tweezer transport using Lewis-Riesenfeld trajectories from section 3.3.

When repeating this simulation with a smaller timestep of $\Delta t = 1 \times 10^{-4}\,\mathrm{T_h} = 1.24\,\mathrm{ns}$, P_{Cs} and the equivalent ground state occupation probability for Rb P_{Rb}, take very similar values to those in fig. 4.4(i), despite the much small Cs trap frequency deviations of less than ± 0.025 %. The results for this simulation have been included in section G.2 of appendix G and table F.3 of appendix F.

These results indicate that the larger t_f values required to obtain the same value for P_{Cs} compared to the single tweezer transport case, are not a result of the suboptimal

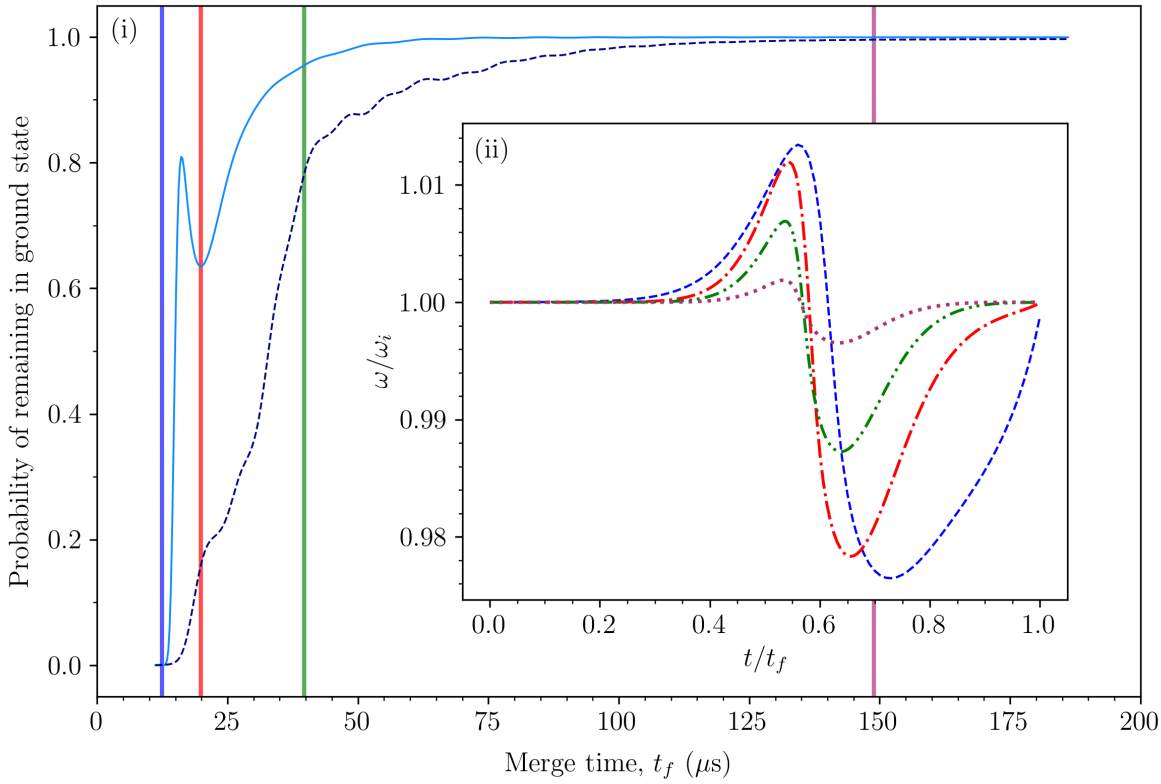

Figure 4.4: (i) Results obtained by moving the 938 nm optical tweezer using a non-rigid Lewis-Riesenfeld trajectory while changing the 938 nm tweezer beam power so the frequency of the effective potential for the Cs atom remains approximately constant. The solid, pale blue line gives the Cs atom ground state occupation probability after the tweezer merge P_{Cs}, while the dashed navy line gives this for the Rb atom P_{Rb}. The four coloured, vertical lines give the merge times t_f corresponding to the trap frequencies shown in (ii). (ii) How the Cs harmonic trap frequency ω changes during a selection of transports with different values for t_f. Here ω_i is the initial trap frequency experienced by the Cs atom. The dashed blue line shows how ω changes for $t_f = 12.4\,\mu$s (blue vertical line in (i)), the red dash-dotted line corresponds to $t_f = 19.8\,\mu$s (red line in (i)), the green dash-double-dotted line to $t_f = 39.7\,\mu$s (green line in (i) and the purple dotted line to $t_f = 148.9\,\mu$s.

trap frequency control. We believe that they instead result from a combination of the Cs atom trap depth reduction, asymmetry of the effective potential during the merge and errors in the trap frequency determined using eq. (4.1.5) due to the difference between the tweezer and Cs potential minimum positions. These factors all contribute to making our approximation of the effective potential as a harmonic potential less applicable. In turn, this limits the applicability of the Lewis-Riesenfeld boundary condition results we use hence resulting in these larger values for t_f. We have included an animation visually demonstrating this in section E.5.1. These effects will also contribute to the similarity between the results obtained for the different trajectories we tested in section 4.2.

In fig. 4.4(i), we see that $P_{\mathrm{Rb}} < P_{\mathrm{Cs}}$ for all values of t_f we tested. This results in the combined ground state occupation probability $P_{\mathrm{combined}} = P_{\mathrm{Cs}} \times P_{\mathrm{Rb}}$ only exceeding 99 % for $t_f > 115.6\,\mu$s despite P_{Cs} exceeding this threshold for $t_f = 54.8\,\mu$s. This suggests that it may now be more fruitful to develop methods to increase P_{Rb} instead of attempting to overcome the limitations discussed above which contribute to lower values of P_{Cs} in the tweezer merging process compared to the single tweezer transport results.

Chapter 5
Concluding remarks

In this work, we have explored a number of methods to increase the probability of maintaining both Cs and Rb atoms in their ground states after merging their optical tweezers. We found that the single most effective method for achieving this is to compensate for the deviation of the Cs potential minimum location from the position of the 938 nm optical tweezer using eq. (4.1.2). Completing this compensation procedure allowed us to reduce the merging time by more than half whilst maintaining a combined probability of greater than 99 % that both atoms remain in their ground state after the merge.

Furthermore, we saw that there is only a small benefit in choosing a merging trajectory for the 938 nm tweezer such that only the Lewis-Riesenfeld boundary conditions for $r_c(t)$ (eqs. (1.2.10), (1.2.12) and (1.2.14)) are satisfied. The Lewis-Riesenfeld boundary conditions on $\rho(t)$ (eqs. (1.2.11), (1.2.13) and (1.2.15)) can be satisfied by adjusting the beam power of the 938 nm optical tweezer throughout the merging process. We found that this allowed us to further reduce the merging time by 20 % whilst still exceeding a combined 99 % ground state probability for both atoms. When applying this method, the Cs ground state occupation probability following the merge becomes greater than the equivalent probability for the Rb atom held in the stationary 814 nm tweezer.

Whilst we have identified improved methods to transport the Cs atom during the tweezer merging process, the excitations of the Rb atom during the merge have now become a significant factor limiting the merging time. A useful next step would be to establish methods to increase the Rb ground state occupation probability whilst minimising the effect on the equivalent Cs probability. A possible way to achieve this might involve decreasing the Cs trap frequency during the merge whilst still satisfying the Lewis-Riesenfeld boundary conditions on $\rho(t)$. This could be implemented by decreasing the 938 nm tweezer beam power near the end of the merge which should reduce the Rb motional excitations.

Only a single radial component of the asymmetric Gaussian tweezer potentials has been considered in this work. As such, we cannot exclude the possibility that effects resulting from the axial and other radial potential component might significantly influence the merging process. Expanding our simulations to incorporate these additional potential components (potentially utilising the short iterative Lanczos method described in appendix D) would allow us to understand the effects of these.

We have assumed that we will be able to find an appropriate Feshbach resonance such that the Cs and Rb interspecies interactions can be tuned to zero. It would be interesting to consider the effects of non-zero interactions between the atoms on the merging process and explore the possibility of using them to further optimise the merging process.

Overall, it is likely that implementing the techniques we describe in this report will allow a significant reduction in the tweezer merging times in our Cs-Rb system. Additionally, we believe that applying these same techniques in other optical tweezers systems utilising different atoms is similarly likely to reduce the minimum merging times.

Bibliography

[1] L. R. Liu et al., Science **360**, 900–903 (2018).
[2] S. Ospelkaus et al., Science **327**, 853–857 (2010).
[3] M. McDonald et al., Nature **535**, 122–126 (2016).
[4] M. R. Tarbutt, B. E. Sauer, J. J. Hudson and E. A. Hinds, New J. Phys. **15**, 053034 (2013).
[5] ACME Collaboration, V. Andreev et al., Nature **562**, 355–360 (2018).
[6] D. DeMille, Phys. Rev. Lett. **88**, 067901 (2002).
[7] J. A. Blackmore et al., Quantum Sci. Technol. **4**, 014010 (2018).
[8] L. D. Carr, D. DeMille, R. V. Krems and J. Ye, New J. Phys. **11**, 055049 (2009).
[9] J. Doyle, B. Friedrich, R. V. Krems and F. Masnou-Seeuws, Eur. Phys. J. D **31**, 149–164 (2004).
[10] E. S. Shuman, J. F. Barry and D. DeMille, Nature **467**, 820–823 (2010).
[11] S. Ding et al., Phys. Rev. X **10**, 021049 (2020).
[12] J. M. Hutson and P. Soldán, Int. Rev. Phys. Chem. **25**, 497–526 (2006).
[13] L. R. Liu et al., Phys. Rev. X **9**, 021039 (2019).
[14] K. Bergmann, H. Theuer and B. W. Shore, Rev. Mod. Phys. **70**, 1003–1025 (1998).
[15] P. K. Molony et al., Phys. Rev. Lett. **113**, 255301 (2014).
[16] N. Schlosser, G. Reymond, I. Protsenko and P. Grangier, Nature **411**, 1024–1027 (2001).
[17] D. J. Wineland and W. M. Itano, Phys. Rev. A **20**, 1521–1540 (1979).
[18] A. Kerman, 'Raman sideband cooling and cold atomic collisions in optical lattices', PhD thesis (Stanford University, Jan. 2002).
[19] T. Köhler, K. Góral and P. S. Julienne, Rev. Mod. Phys. **78**, 1311–1361 (2006).
[20] L. R. Liu et al., *Ultracold molecular assembly*, 2017, arXiv:1701.03121 [physics.atom-ph].
[21] D. Barredo et al., Science **354**, 1021–1023 (2016).
[22] M. Endres et al., Science **354**, 1024–1027 (2016).
[23] S. Chu, J. E. Bjorkholm, A. Ashkin and A. Cable, Phys. Rev. Lett. **57**, 314–317 (1986).
[24] A. L. Migdall et al., Phys. Rev. Lett. **54**, 2596–2599 (1985).
[25] R. Grimm, M. Weidemüller and Y. B. Ovchinnikov, 'Optical dipole traps for neutral atoms', in , Vol. 42, edited by B. Bederson and H. Walther, Advances In Atomic, Molecular, and Optical Physics (Academic Press, 2000), pp. 95–170.
[26] E. L. Raab et al., Phys. Rev. Lett. **59**, 2631–2634 (1987).
[27] S. Chu, Rev. Mod. Phys. **70**, 685–706 (1998).
[28] D. G. Grier, Nature **424**, 810–816 (2003).
[29] J. P. Gordon and A. Ashkin, Phys. Rev. A **21**, 1606–1617 (1980).
[30] A. Ashkin, Phys. Rev. Lett. **25**, 1321–1324 (1970).
[31] A. Ashkin and J. P. Gordon, Opt. Lett. **4**, 161–163 (1979).
[32] D. A. Steck, *Alkali D line data*, (2019) https://steck.us/alkalidata/ (visited on 01/04/2021).
[33] J. E. Bjorkholm, R. R. Freeman, A. Ashkin and D. B. Pearson, Opt. Lett. **5**, 111–113 (1980).
[34] J. Dalibard and C. Cohen-Tannoudji, J. Opt. Soc. Am. B **2**, 1707–1720 (1985).
[35] R. V. Brooks et al., *Preparation of one ^{87}Rb and one ^{133}Cs atom in a single optical tweezer*, 2021, arXiv:2104.05760 [physics.atom-ph].
[36] B. Ueberholz et al., J. Phys. B: At. Mol. Opt. Phys. **35**, 4899–4914 (2002).
[37] D. Guéry-Odelin et al., Rev. Mod. Phys. **91**, 045001 (2019).
[38] M. R. Lam et al., Phys. Rev. X **11**, 011035 (2021).
[39] W. C. Campbell et al., Phys. Rev. Lett. **105**, 090502 (2010).
[40] V. M. Schäfer et al., Nature **555**, 75–78 (2018).

[41]H. R. Lewis and W. B. Riesenfeld, J. Math. Phys. **10**, 1458–1473 (1969).
[42]E. Torrontegui et al., Phys. Rev. A **83**, 013415 (2011).
[43]H. R. Lewis and P. G. L. Leach, J. Math. Phys. **23**, 2371–2374 (1982).
[44]A. Tobalina, M. Palmero, S. Martínez-Garaot and J. G. Muga, Sci. Reports **7**, 5753 (2017).
[45]L. Liu, 'Building single molecules – reactions, collisions, and spectroscopy of two atoms', PhD thesis (Harvard University, May 2019).
[46]M. S. Safronova, B. Arora and C. W. Clark, Phys. Rev. A **73**, 022505 (2006).
[47]W. H. Press, S. A. Teukolsky, W. T. Vetterling and B. P. Flannery, *Numerical recipes: the art of scientific computing*, 3rd ed. (Cambridge University Press, Cambridge, 2007).
[48]W. M. Haynes, ed., *CRC Handbook of Chemistry and Physics*, 97th ed. (CRC Press, Boca Raton, 2016).
[49]D. J. Tannor, *Introduction to quantum mechanics: a time-dependent perspective* (University Science Books, 2006).
[50]C. Leforestier et al., J. Comput. Phys. **94**, 59–80 (1991).
[51]W. Magnus, Commun. on Pure Appl. Math. **7**, 649–673 (1954).
[52]E. Koch, 'The Lanczos method', in *The LDA+DMFT approach to strongly correlated materials*, Vol. 1, edited by A. Lichtenstein, Modeling and Simulation (Forschungszentrum Jülich, 2011) Chap. 8.
[53]B. I. Schneider et al., 'Recent advances in computational methods for the solution of the time-dependent Schrödinger equation for the interaction of short, intense radiation with one and two electron systems', in *Quantum dynamic imaging: theoretical and numerical methods*, edited by A. D. Bandrauk and M. Ivanov (Springer New York, New York, NY, 2011), pp. 149–208.
[54]H. Gharibnejad, B. Schneider, M. Leadingham and H. Schmale, Comput. Phys. Commun. **252**, 106808 (2020).
[55]L. Euler, Acta Acad. scientiarum imperialis petropolitanae, 29–51 (1783).
[56]R. M. Corless et al., Adv. Comput. Math. **5**, 329–359 (1996).
[57]G. A. Kalugin, 'Analytical properties of the Lambert W function', PhD thesis (The University of Western Ontario, 2011).
[58]T. Hänsch and A. Schawlow, Opt. Commun. **13**, 68–69 (1975).
[59]S. Chu et al., Phys. Rev. Lett. **55**, 48–51 (1985).
[60]K. F. Riley, M. P. Hobson and S. J. Bence, *Mathematical methods for physics and engineering*, 3rd ed. (Cambridge University Press, Cambridge, 2006).
[61]R. Dum, P. Marte, T. Pellizzari and P. Zoller, Phys. Rev. Lett. **73**, 2829–2832 (1994).
[62]P. D. Lett et al., Phys. Rev. Lett. **61**, 169–172 (1988).
[63]J. Dalibard and C. Cohen-Tannoudji, J. Opt. Soc. Am. B **6**, 2023–2045 (1989).
[64]M. Kasevich and S. Chu, Phys. Rev. Lett. **69**, 1741–1744 (1992).
[65]V. Vuletić, C. Chin, A. J. Kerman and S. Chu, Phys. Rev. Lett. **81**, 5768–5771 (1998).
[66]A. M. Kaufman, B. J. Lester and C. A. Regal, Phys. Rev. X **2**, 041014 (2012).
[67]Y. Yu et al., Phys. Rev. A **97**, 063423 (2018).
[68]N. R. Hutzler, L. R. Liu, Y. Yu and K.-K. Ni, New J. Phys. **19**, 023007 (2017).
[69]C. C. Gerry and P. L. Knight, *Introductory quantum optics* (Cambridge University Press, Cambridge, 2005).
[70]N. Schlosser, G. Reymond and P. Grangier, Phys. Rev. Lett. **89**, 023005 (2002).
[71]M. O. Brown et al., Phys. Rev. X **9**, 011057 (2019).
[72]T. Grünzweig, A. Hilliard, M. McGovern and M. F. Andersen, Nat. Phys. **6**, 951–954 (2010).
[73]B. J. Lester et al., Phys. Rev. Lett. **115**, 073003 (2015).
[74]G. Strang, SIAM journal on numerical analysis **5**, 506–517 (1968).

Appendix A
Cooling

In order to cool atoms to their motional ground state, a number of different cooling techniques are applied in sequence. In this appendix, we will explore the basic theory behind Doppler cooling and Raman sideband cooling.

A.1 Doppler cooling

Doppler cooling was the first proposed method of cooling atoms using laser light. In this process, atoms are exposed to laser radiation with a small red-detuning, such that when the atoms move towards the radiation source the observed radiation frequency is Doppler shifted to match that of an atomic transition. The resultant absorption events will reduce the magnitude of the atoms momentum by the photon momentum $\hbar k$, where $k = \frac{2\pi}{\lambda}$ is the photon wavenumber, thus producing a damping effect.[58] Counter-propagating laser beams can be set-up along the three Cartesian axes to produce a damping effect in three dimensions and provide some confinement due to the collective radiation pressure.[59]

For each absorption event, there will be a corresponding spontaneous emission at a later time. This will result in the emission of a photon in a random direction, thus leading to the heating effect described in section 1.1.2 and imposing a limit on the temperature to which atoms can be cooled. This limit is called the Doppler temperature and can be found to be

$$T_D = \frac{\hbar\Gamma}{2k_B}, \tag{A.1.1}$$

where Γ is the linewidth of the transition.[27]

For species to be appreciably cooled, they must repeatedly scatter photons. As such, species cooled using this method usually have a high probability of returning to their initial state by the spontaneous emission.[58] Directly laser cooling molecules is thus difficult since they have a much more complicated energy level structure than atoms so there is usually a low probability that the molecule will return to its original state following the spontaneous emission.[10,11]

A.2 Bound atoms

When atoms are bound within a trap, near monochromatic laser radiation may appear to be comprised of more than one frequency in the frame of the trapped atom and the atomic emission spectrum in the laboratory frame will similarly show multiple frequencies for each transition. The origin of this effect can be seen using a classical model of a harmonically bound, two-level atomic system as described by Wineland and Itano.[17]

The harmonic trap oscillation frequencies in each Cartesian direction $\{\Omega_i\}$ where $i \in \{x, y, z\}$ are assumed to be small in comparison to the atomic transition frequency ω_0, that is $\{\Omega_i\} \ll \omega_0 \; \forall \, i$. Additionally, we will only consider the strong binding case where $\Gamma \ll \{\Omega_i\} \; \forall \, i$ for Γ the natural linewidth of the transition.

Without loss of generality, consider the atom oscillating with amplitude x_A in the x direction such that its position is

$$x = x_A \sin(\Omega_x t). \tag{A.2.1}$$

Similarly, consider an incident electromagnetic wave along the x axis with wavenumber k and frequency ω, where the electric field component is given by

$$\mathbf{E} = \mathbf{E}_0 \sin(kx - \omega t), \tag{A.2.2}$$

such that there is no phase difference between the atomic motion and the electric field oscillations.

The resultant electric field experienced by the atom is thus

$$\mathbf{E}_{\text{eff}} = \mathbf{E}_0 \sin\big(kx_A \sin(\Omega_x t) - \omega t\big). \tag{A.2.3}$$

By using

$$\cos\big(x\sin(\theta)\big) = \sum_{n=-\infty}^{\infty} J_n(x)\cos(n\theta), \tag{A.2.4}$$

$$\sin\big(x\sin(\theta)\big) = \sum_{n=-\infty}^{\infty} J_n(x)\sin(n\theta), \tag{A.2.5}$$

where the $J_n(x)$ are Bessel functions of the first kind and $n \in \mathbb{Z}$,[60] we can expand $\mathbf{E}_{\text{eff}}$ in terms of Bessel functions to yield

$$\mathbf{E}_{\text{eff}} = \sum_{n=-\infty}^{\infty} J_n(kx_A)\sin\big((n\Omega_x - \omega)t\big). \tag{A.2.6}$$

This demonstrates that the effective radiation field seen by the atom consists of discrete modes at frequencies $\omega - n\Omega_x$ where the amplitudes are given by $J_n(kx_A)$ as shown in fig. A.1. The radiation emitted by the atom will have a similar spectrum, but with each mode broadened by the natural lifetime Γ, thus in the case of weak binding $\Gamma \gtrsim \{\Omega_i\}$ the individual spectral lines for $n \neq 0$ (known as *sidebands*) will not be distinguishable.

In the strong binding case, tuning the cooling laser frequency to the first resolved lower sideband with frequency $\omega - \Omega_x$ can be used to cool the atom. This process works since, on average, the photon emitted via spontaneous emission will be emitted at the central transition frequency ω (or *carrier frequency*), hence leading to a net reduction in the energy of the atom.[17] By interpreting the sidebands as occurring due to the vibrational modes of the atom ion the trap, this cooling process can be interpreted as an anti-Stokes transition leading to the reduction in the vibrational energy of the atom.[18]

In this interpretation, when the atom is cooled to its motional ground state, the lower sideband will disappear since there will be no lower vibrational levels. In the case that the sidebands are well-resolved, the cooling radiation will now only interact weakly with the ground-state atoms, thus reducing any subsequent heating due to spontaneous emission processes. Such a state is known as a *dark state*.[61]

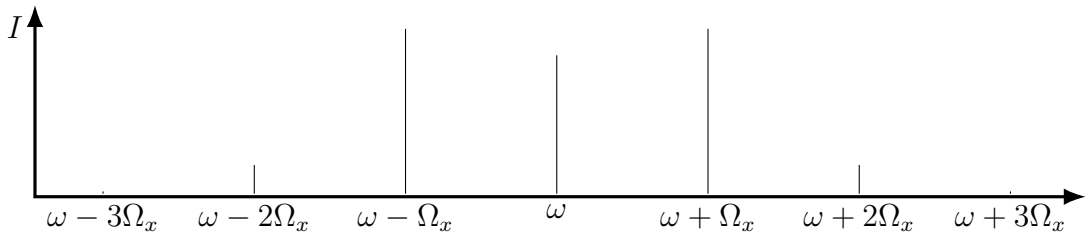

Figure A.1: The effective radiation spectrum seen by a bound atom in a harmonic trap. The electric field component of the incoming radiation is taken to be in-phase and collinear to the oscillation of the bound atom as shown in eqs. (A.2.1) and (A.2.2) in the strong binding case of $\Gamma \ll \{\Omega_i\}\ \forall\, i$. As depicted in the figure, the atom sees the radiation at the discrete frequencies $\omega + n\Omega_x$, where ω is the electronic transition frequency, Ω_x is the trap frequency and $n \in \mathbb{Z}$. The intensities I of these spectral lines are given by the first kind of Bessel functions $J_n(kx_A)^2$ and here we have plotted the case of $kx_A = 1.5$. The atomic emission spectrum in the laboratory frame will look similar to the spectrum shown, however each spectral line will be broadened with a full width at half maximum (FWHM) given by the natural linewidth Γ for the transition.

A.3 Raman sideband cooling

Methods other than Doppler cooling must be used to cool atoms below the Doppler temperature to their motional ground state. The first sub-Doppler cooling of neutral atoms was achieved using polarisation gradient cooling (which we will not discuss here), however this cooling method is instead limited by the photon recoil temperature[62,63]

$$T_R = \frac{\hbar^2 k^2}{2k_B M}, \tag{A.3.1}$$

where M is the atomic mass and $\hbar k$ is the momentum of the cooling photons. Raman sideband cooling utilises a dark state (discussed in section A.2) to cool below the recoil temperature.[64]

For neutral atoms in dipole traps, it is difficult to achieve the high trap strength required to resolve the motional sidebands discussed in section A.2, so an alternative method is used. Instead of relying on a large trap strength, a two-photon Raman transition is stimulated between two stable or long-lived electronic states $|2\rangle \leftarrow |1\rangle$ before optically pumping the atom back to the initial state $|1\rangle$ via spontaneous emission from an additional state $|3\rangle$ as shown in fig. A.2. The lifetime of the intermediate state $|2\rangle$ can be altered by controlling the time at which the optical pumping occurs thus allowing the vibrational sidebands of this state to be well-resolved.[18,65]

The stimulated Raman transition $|2\rangle \leftarrow |1\rangle$ can be achieved using two counter-propagating lasers with frequencies ω_{l1} and ω_{l2} such that

$$\omega_{l1} - \omega_{l2} = \omega_{12} + \Delta, \tag{A.3.2}$$

where ω_{12} is the $|2\rangle \leftarrow |1\rangle$ transition frequency and $\Delta < 0$ is a red-detuning. Changing the magnitude of Δ and the lifetime of $|2\rangle$ allows specific vibrational transitions to be targeted to optimise the cooling process.[64,65]

For this cooling technique to be successful, the optical pumping step must preserve the lowered vibrational state achieved using the $|2\rangle \leftarrow |1\rangle$ Raman transition. The probability

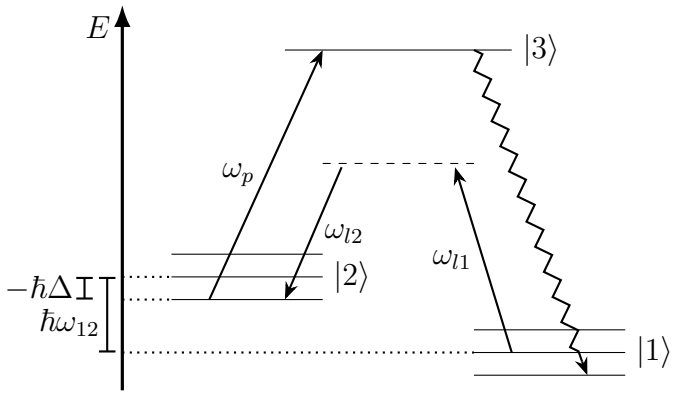

Figure A.2: Electronic transitions in Raman sideband cooling. Arrows represent photons being absorbed/emitted and horizontal lines represent atomic states. In particular, the dashed horizontal line is the virtual Raman state and the groups of horizontal lines next to the electronic state labels $|1\rangle$ and $|2\rangle$ represent different vibrational states of the trap when the atom is in these electronic states. In the cooling process, the atom is initially in a non-ground vibrational state within $|1\rangle$. Counter-propagating laser beams at frequencies ω_{l1} and ω_{l2} cause the two-photon, anti-Stokes Raman transition into a lower vibrational state of $|2\rangle$ which is selected using the detuning Δ of $\omega_{l1} - \omega_{l2}$ from the Stokes scattering frequency ω_{12}. At a later time, radiation of frequency ω_p is used to optically pump the atom back to a lower vibrational state of $|1\rangle$ via the spontaneous emission from $|3\rangle$, hence leading to a cooling effect.

of vibrational excitation during the optical pumping process is proportional to

$$p_{\text{ext}} = (2\bar{n} + 1)\frac{k_B T_R}{\hbar\Omega} = (2\bar{n} + 1)\eta^2, \tag{A.3.3}$$

where $\bar{n}$ is the average vibrational quantum number, T_R is the recoil temperature defined in eq. (A.3.1) for the pumping photons, Ω is the relevant trap frequency and $\eta = \sqrt{k_B T_R/\hbar\Omega}$ is known as the Lamb-Dicke parameter.[18,66] Due to this, atoms should initially be cooled into the Lamb-Dicke regime (where $\eta \ll 1$) using other cooling techniques before Raman sideband cooling is used.

The ground motional state of $|1\rangle$ can be made a dark state by choosing ω_{l1}, ω_{l2} and the optical pumping transition frequency ω_p such that they are well-separated from the resonance frequencies for likely electronic transitions from $|1\rangle$.[64] This allows the accumulation of a significant motional ground state atomic population and populations of around 90 % have been reported.[66,67]

A.4 Cooling atoms in optical dipole traps

Due to the small trap depths of optical dipole traps and the heating processes described in section 1.1.2, atoms in optical dipole traps must be continually cooled for trapping to be maintained. This is complicated by the fact that it is not possible to apply near-resonant Doppler cooling radiation at the same time as the optical dipole trapping radiation since it will cause increased dipole heating. The AC Stark shift in the atomic energy levels caused by the trapping radiation will also greatly reduce the cooling efficiency.[29,68] These problems can be avoided by alternating between applying the trapping radiation and counter-propagating cooling lasers.[23] In this procedure, loss is minimised since the radiation pressure of the cooling beams (arising due to the scattering force) keeps the atoms sufficiently confined whilst the trapping beams are switched off.[59]

Naturally, this issue does not affect the Raman sideband cooling technique described in

section A.3 which relies on atoms being confined within optical tweezers. This thus allows the continual cooling of the atoms via Raman sideband cooling whilst they are kept isolated in their own tweezers. However, after the tweezers have been merged and both atoms occupy the same tweezer Raman sideband cooling cannot be easily performed. This is since it will stimulate light-assisted collisions and lead to loss by the process discussed in appendix C.

Appendix B
Dressed atom derivation of the dipole force

In section 1.1.1, the properties of the dipole force were derived from a conservative potential by approximating the atom as a simple harmonic oscillator. From a more fundamental perspective, the origins of the dipole force can be explored by utilising a dressed atom approach (where the eigenstates of the combined atom and radiation field system are considered). In this appendix, the properties of the dipole force will be derived by broadly following the derivation presented by Dalibard and Cohen-Tannoudji.[34]

B.1 Derivation

Consider the two level atomic system with ground state $|g\rangle$ and excited state $|e\rangle$ separated by an energy $\hbar\omega_0$ within a single mode radiation field of frequency ω, as shown in fig. B.1.

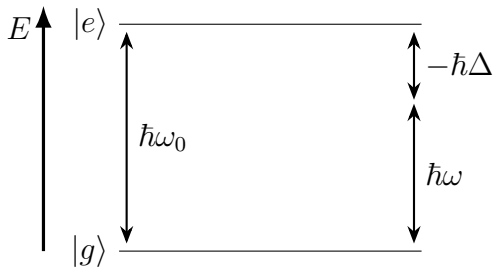

Figure B.1: Energy levels of a bare two-level atom. ω_0 is the transition frequency between the two atomic levels, ω is the frequency of the radiation field and $\Delta = \omega - \omega_0$ is the detuning of the radiation field from the transition frequency.

The Hamiltonian of such a system is given by

$$\hat{H} = \hat{H}_{\mathrm{A}} + \hat{H}_{\mathrm{F}} + \hat{H}_{\mathrm{int}}, \tag{B.1.1}$$

where $\hat{H}_{\mathrm{A}}$ is the Hamiltonian the atom, $\hat{H}_{\mathrm{F}}$ is the Hamiltonian of the field and $\hat{H}_{\mathrm{int}}$ is the atom-field interaction term. By evaluating at a single point $\mathbf{r}$ we can neglect the atomic kinetic energy term to give

$$\hat{H}_{\mathrm{A}} = \hbar\omega_0 \left|e\right\rangle\!\left\langle e\right| = \hbar\omega_0 \hat{\sigma}_+ \hat{\sigma}_-, \tag{B.1.2}$$

by defining the raising operator $\hat{\sigma}_+ = \left|e\right\rangle\!\left\langle g\right|$ and the lowering operator $\hat{\sigma}_- = \hat{\sigma}_+^\dagger$ where $\hat{q}^\dagger$ denotes acting with the adjoint operation on the operator $\hat{q}$.

By setting the vacuum zero point energy to zero, the single mode field Hamiltonian can be given by

$$\hat{H}_F = \hbar\omega \hat{a}^\dagger \hat{a}, \tag{B.1.3}$$

where $\hat{a}$ and $\hat{a}^\dagger$ are the field mode annihilation and creation operators respectively. These are defined by $\hat{a}^\dagger \left|n\right\rangle = \sqrt{n+1}\left|n+1\right\rangle$ and $\hat{a}\left|n+1\right\rangle = \sqrt{n+1}\left|n\right\rangle$ where $\left|n\right\rangle$ is the n photon number state for the radiation field.

In the electric dipole approximation the interaction term can be written as[69]

$$\hat{H}_{\text{int}} = \hat{\mathbf{d}} \cdot \hat{\mathbf{E}}(t), \tag{B.1.4}$$

where $\hat{\mathbf{d}} = e\mathbf{r}$ is the electric dipole operator and $\hat{\mathbf{E}}(t) = \vec{\mathcal{E}}(\mathbf{r})\hat{a} + \vec{\mathcal{E}}^*(\mathbf{r})\hat{a}^\dagger$ is the electric field operator for a single mode field where $\vec{\mathcal{E}}(\mathbf{r}) \in \mathbb{C}^3$.

Using $\langle e|\hat{\mathbf{d}}|e\rangle = \langle g|\hat{\mathbf{d}}|g\rangle = 0$, we can rewrite

$$\hat{\mathbf{d}} = \vec{\mu}\hat{\sigma}_- + (\vec{\mu}\hat{\sigma}_-)^\dagger = \vec{\mu}(\hat{\sigma}_+ + \hat{\sigma}_-), \tag{B.1.5}$$

for $\vec{\mu} \in \mathbb{R}^3$. So, we have

$$\hat{H}_{\text{int}} = \big(\vec{\mu}(\hat{\sigma}_+ + \hat{\sigma}_-)\big) \cdot \Big(\vec{\mathcal{E}}\,\hat{a} + \vec{\mathcal{E}}^*\hat{a}^\dagger\Big). \tag{B.1.6}$$

By considering the time evolution of these operators in the interaction picture and applying the rotating wave approximation to remove the quickly oscillating terms, this can be simplified to give

$$\hat{H}_{\text{int}} = \vec{\mu} \cdot \Big(\vec{\mathcal{E}}^*\hat{\sigma}_-\hat{a}^\dagger + \vec{\mathcal{E}}\,\hat{\sigma}_+\hat{a}\Big). \tag{B.1.7}$$

Putting eqs. (B.1.2), (B.1.3) and (B.1.7) together yields the Hamiltonian

$$\hat{H} = \hbar(\omega - \Delta)\hat{\sigma}_+\hat{\sigma}_- + \hbar\omega\hat{a}^\dagger\hat{a} + \vec{\mu} \cdot \Big(\vec{\mathcal{E}}^*\hat{\sigma}_-\hat{a}^\dagger + \vec{\mathcal{E}}\,\hat{\sigma}_+\hat{a}\Big), \tag{B.1.8}$$

where $\Delta = \omega - \omega_0$ is the detuning of the field radiation from the atomic resonance.

Considering the basis states $|g\rangle \otimes |n+1\rangle = |g, n+1\rangle$ and $|e\rangle \otimes |n\rangle = |e, n\rangle$, it is clear that the matrix element due to $\hat{H}_{\text{int}}$ is only non-zero for the off-diagonal terms

$$\langle e, n|\hat{H}_{\text{int}}|g, n+1\rangle = \sqrt{n+1}\Big(\vec{\mu} \cdot \vec{\mathcal{E}}\Big) = \frac{\hbar}{2}\omega_r(\mathbf{r})\exp\big(i\phi(\mathbf{r})\big), \tag{B.1.9}$$

for $\omega_r(\mathbf{r})$ the Rabi frequency when $\Delta = 0$ and $\phi(\mathbf{r})$ some phase. This relation can be determined by solving the Schrödinger equation for the basis state occupation probabilities in the case of $\Delta = 0$.

Using this result, $\hat{H}$ in terms of the basis states can be represented in matrix form as

$$\hat{H} = \hbar\begin{pmatrix} (n+1)\omega & \frac{1}{2}\omega_r e^{-i\phi} \\ \frac{1}{2}\omega_r e^{i\phi} & (n+1)\omega - \Delta \end{pmatrix}. \tag{B.1.10}$$

By solving for the eigenvalues of this matrix, the energies of the eigenstates are found to be

$$E_{n,\pm} = \hbar\left((n+1)\omega - \frac{\Delta}{2} \pm \frac{\Omega^2(\mathbf{r})}{2}\right), \tag{B.1.11}$$

where

$$\Omega(\mathbf{r}) = \sqrt{\omega_r^2(\mathbf{r}) + \Delta^2}, \tag{B.1.12}$$

is the Rabi frequency.

For the treatment above, the radiation field is assumed to initially be in a coherent state, hence the photons are distributed according to Poissonian statistics. It is then assumed that the standard deviation of the photon distribution Δn satisfies $\Delta n \ll n$, thus n can be taken to have a definite value.

In the case where the coupling between the atom and field is zero ($\vec{\mu} = \mathbf{0}$), the Hamiltonian eigenstates are equivalent to the states $|g, n+1\rangle$ and $|e, n\rangle$ (i.e. the atomic states in the presence of an n or $n+1$ photon field) with the energy difference between these states given by $\hbar|\Delta|$ as shown in fig. B.2a. These are the *bare states*. For a non-zero atom-field coupling, the eigenstates $|n, -\rangle$ and $|n, +\rangle$ (the *dressed states*) are described by some linear superposition of the bare states with the difference in energy between these states given by $\hbar\Omega(\mathbf{r})$ as shown in fig. B.2b. Where the detuning is zero, the dressed states will remain non-degenerate, however the bare states will be degenerate.

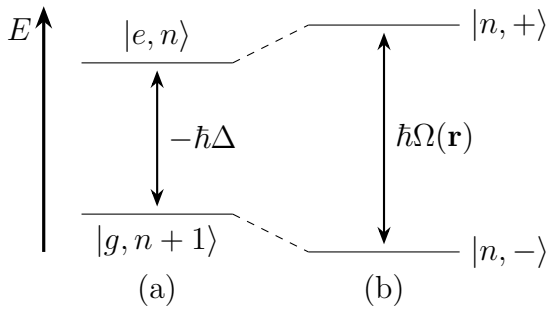

Figure B.2: Energy of combined atom-field system in cases of zero and non-zero coupling. If the atom-field coupling is zero ($\vec{\mu} = \mathbf{0}$) the eigenstates are the *bare states* $|g, n+1\rangle$ and $|e, n\rangle$ which differ in energy by the detuning $\hbar|\Delta|$ as shown for the $\Delta < 0$ case in (a). For a non-zero atom-field coupling, the *dressed states* $|n, -\rangle$ and $|n, +\rangle$ are the system eigenstates which have a non-trivial dependence on the bare states and differ in energy by the Rabi frequency $\hbar\Omega(\mathbf{r})$ as shown in (b).

As demonstrated in eqs. (B.1.9), (B.1.11) and (B.1.12), the magnitude of the energy splitting will depend on the atom-field coupling. In a radiation field where the intensity is non-uniform in space, this will result in the dressed state energies being dependent on the spatial position of the atom. This is illustrated in fig. B.3 in the case where an atom is moved across a Gaussian laser beam.

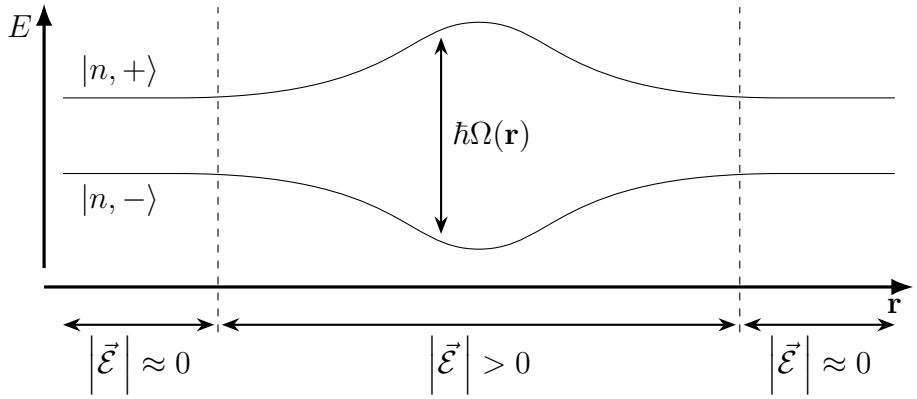

Figure B.3: Dressed state energy levels across a Gaussian laser beam. As the atom transits a laser beam with intensity $\left|\vec{\mathcal{E}}\right|^2$ following a Gaussian profile, the energies of the dressed states $|n, +\rangle$ and $|n, -\rangle$, given by eq. (B.1.11) follow the radiation intensity profile.

It can be shown that the mean dipole force potential experienced by a stationary atom can be written as[34]

$$U = \Pi_+ E_+ + \Pi_- E_-, \tag{B.1.13}$$

where Π_+ and Π_- are the equilibrium populations of the $|n,+\rangle$ and $|n,-\rangle$ states respectively while $E_+ = \frac{1}{2}(E_{n,+} - E_{n,-}) = \frac{1}{2}\hbar\Omega(\mathbf{r})$ and $E_- = -E_+ = -\frac{1}{2}\hbar\Omega(\mathbf{r})$ are the differences of the energies of these states from the mean energy $\frac{1}{2}(E_{n,+} + E_{n,-})$ for each fixed n.

The equilibrium populations $\Pi_\pm$ depend on the rates for spontaneous emission from the $|n,+\rangle$ and $|n,-\rangle$ states to the $|n-1,+\rangle$ and $|n-1,-\rangle$ states. Naturally, these will depend on the relative contributions of the $|e,n\rangle$ and $|g,n+1\rangle$ bare states to each dressed states since spontaneous emission is only possible from the excited atomic state. Since the lower energy bare state will have a greater contribution to $|n,-\rangle$ (and vice-versa for $|n,+\rangle$) the sign of the detuning Δ will dictate the relative magnitudes of the $\Pi_\pm$ as it gives the energy ordering of the bare states.

For a red detuned trap ($\Delta < 0$), $|g,n+1\rangle$ will be lower in energy than $|e,n\rangle$, thus $\Pi_- > \Pi_+$ due to the greater rate of spontaneous emission from the $|n,+\rangle$ compared to $|n,-\rangle$. Using eq. (B.1.13), this will thus result in an attractive potential within the radiation beam. In contrast, a blue detuned trap ($\Delta > 0$) will instead result in a repulsive potential due to the greater population of the $|n,+\rangle$ states compared to the $|n,-\rangle$ states ($\Pi_+ > \Pi_-$) since the $|e,n\rangle$ bare states will be lower in energy than the $|g,n+1\rangle$ states. This describes the same trap behaviour as that found by modelling the atom as a simple harmonic oscillator as described in section 1.1.1 with eq. (B.1.13) analogous to eq. (1.1.1).

B.2 Dipole force heating

In the previous section, we have seen in that for a stationary atom, the mean dipole force is dependent on the steady state populations of the dressed states. The instantaneous dipole force will similarly depend on the instantaneous system state with the sign of the force dependent on if a dressed state of type $|n,+\rangle$ or $|m,-\rangle$, for $n, m \in \mathbb{N}$, is occupied. Transitions between these two classes of dressed state will hence lead to fluctuations in the sign of the dipole force and a heating effect.[34]

Appendix C
Trapping single atoms

Optical dipole traps with a very small volume and high radiation intensity can be constructed using tightly focussed Gaussian radiation beams. Traps of this type can be used to confine single atoms when the beam waist is of similar order to the wavelength of the trapping light and they are loaded using a MOT containing a low density of atoms.[16] This is achieved since the small trap volume establishes a collisional blockade meaning that there are two possible outcomes when an atom enters the trap region: if the trap is empty, the incident atom is trapped, otherwise it is involved in a two-body collision which causes both atoms to escape from the trap.[70] This process would lead to a loading efficiency of 50 %, however other collisional processes may also occur when applying red-detuned polarisation gradient cooling during the loading. This can lead to a higher mean loading efficiency of 64(1) %.[71]

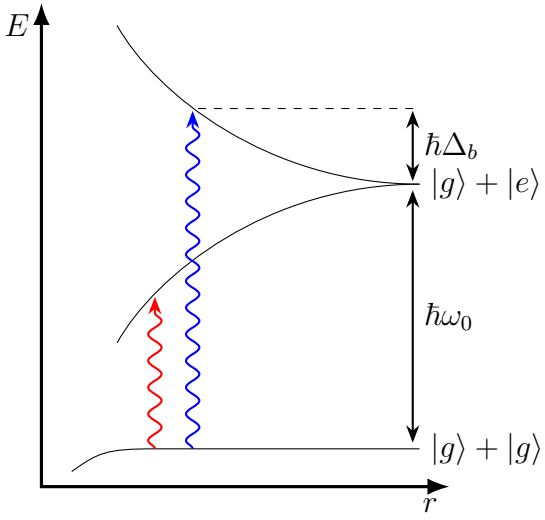

Figure C.1: Illustration of using light-assisted collisions to enhance the probability of loading a single atom in an optical dipole trap. The lower, mostly horizontal, line labelled $|g\rangle + |g\rangle$, represents the nearly constant interatomic interaction potential for two ground state atoms while the two upper lines, labelled with $|g\rangle + |e\rangle$, show the possible potentials when one atom is in an excited electronic state. These potentials illustrate how the combined energy of the two atoms E varies with the interatomic spacing r. When light which is red-detuned from the transition frequency ω_0 is used to excite an atom (the red wavy line), the attractive interatomic potential results causing both atoms to gain considerable kinetic energy which results in the loss of both atoms from the trap. Alternatively, if blue-detuned light, with detuning Δ_b, excites one of the atoms the repulsive potential results. In this case, the maximum kinetic energy increase is given by $\hbar\Delta_b$ which can be chosen to be of similar magnitude to the trap depth giving an increased probability that exactly one atoms will escape from the trap. Adapted from the figure by Grünzweig et al..[72]

During the tweezer loading, light-assisted collisions occur between the atoms. In such collisions, one atom undergoes a transition into an excited state thus altering the interatomic potential between the atoms. By choosing the frequency and intensity of the transition inducing light, the probability that certain interaction potentials will develop can be altered. For example, if blue-detuned light is used, a repulsive interatomic potential is more likely to develop and the kinetic energy transferred within the inelastic collision between the atoms can be controlled using the detuning from the transition frequency as shown in fig. C.1. By making probable kinetic energy transfer in the collision of a similar magnitude to the trap depth, the probability that only a single atom will escape the trap can be increased. Such a technique has been used to increase the single-atom loading probability of ^{87}Rb atoms to 90 %.[73]

Appendix D
Numerical time evolution methods

The time evolution of a wave function $\big|\Psi(\vec{r},t)\big\rangle$ under a Hamiltonian $\hat{H}(\vec{r},t)$ is governed by the Schrödinger equation

$$i\hbar\frac{\mathrm{d}}{\mathrm{d}t}\big|\Psi(\vec{r},t)\big\rangle = \hat{H}(\vec{r},t)\big|\Psi(\vec{r},t)\big\rangle\,. \tag{D.0.1}$$

This can be recast into the Heisenberg picture were the time evolution between some initial time t_i and a final time t_f is given by

$$\begin{aligned}\big|\Psi(t_f)\big\rangle &= \hat{U}(t_f,t_i)\big|\Psi(t_i)\big\rangle \\ \text{where}\quad \hat{U}(t_f,t_i) &:= \exp\left(-\frac{i}{\hbar}\int_{t_i}^{t_f}\hat{H}(t')\,\mathrm{d}t'\right).\end{aligned} \tag{D.0.2}$$

We then split (t_i,t_f) into N subintervals of length $\Delta t = \frac{t_f-t_i}{N}$ with $t_0 = t_i$ and $t_N = t_f$. For N sufficiently large $\hat{H}(t_{k+1}) \approx \hat{H}(t_k)$ for $k \in [0, N-1]$, so[49,50]

$$\hat{U}(t_f,t_i) \approx \prod_{k=0}^{N-1}\exp\left(-\frac{i}{\hbar}\hat{H}(t_k)\Delta t\right). \tag{D.0.3}$$

Numerical methods are then used to approximate $\hat{U}(t_{k+1},t_k)$ which is then applied to the wave function $\big|\Psi(\vec{r},t_k)\big\rangle$ to determine $\big|\Psi(\vec{r},t_{k+1})\big\rangle$ as shown in eq. (D.0.2). Repeated application allows the determination of $\big|\Psi(t_f)\big\rangle$ from $\big|\Psi(t_i)\big\rangle$.

D.1 Split-step method

In the split-step (or split operator) method, we take $\hat{H}(\vec{r},t_k) = \hat{T} + \hat{V}(\vec{r},t_k)$ where $\hat{T}$ and $\hat{V}$ are the kinetic and potential parts of the Hamiltonian respectively. Using this, we write[49,50]

$$\hat{U}(t_{k+1},t_k) = \exp\left(-\frac{i}{\hbar}\Big(\hat{T}+\hat{V}(\vec{r},t_k)\Big)\Delta t\right) = \exp\left(-\frac{i}{\hbar}\hat{T}\Delta t\right)\exp\left(-\frac{i}{\hbar}\hat{V}(\vec{r},t_k)\Delta t\right) + \mathcal{O}\big(\Delta t^2\big). \tag{D.1.1}$$

Here the error term $\mathcal{O}\big(\Delta t^2\big)$ results from the non-commutativity of $\hat{T}$ and $\hat{V}(\vec{r},t_k)$. This error term can be made third order in time by taking the Strang operator splitting[49,74]

$$\begin{aligned}\hat{U}(t_{k+1},t_k) =& \left[\exp\left(-\frac{i}{2\hbar}\hat{V}(\vec{r},t_k)\Delta t\right)\exp\left(-\frac{i}{2\hbar}\hat{T}\Delta t\right)\right] \\ &\cdot\left[\exp\left(-\frac{i}{2\hbar}\hat{T}\Delta t\right)\exp\left(-\frac{i}{2\hbar}\hat{V}(\vec{r},t_k)\Delta t\right)\right] + \mathcal{O}\big(\Delta t^3\big) \\ =& \exp\left(-\frac{i}{2\hbar}\hat{V}(\vec{r},t_k)\Delta t\right)\exp\left(-\frac{i}{\hbar}\hat{T}\Delta t\right)\exp\left(-\frac{i}{2\hbar}\hat{V}(\vec{r},t_k)\Delta t\right) + \mathcal{O}\big(\Delta t^3\big).\end{aligned} \tag{D.1.2}$$

With this form of $\hat{U}(t_{k+1}, t_k)$, it is possible to use fast Fourier transforms (FFTs)[47] to quickly and easily transform between configuration space, where $\hat{V}(\vec{r}, t_k)$ has a diagonal representation, and momentum space, where $\hat{T}$ has a diagonal representation. We illustrate this process in fig. D.1 where each application of $\frac{i}{2\hbar}\hat{V}(\vec{r}, t_k)$ acts as a 'half step' in configuration space while application of $\exp\left(-\frac{i}{\hbar}\hat{T}\Delta t\right)$ in momentum space is a 'full step'.

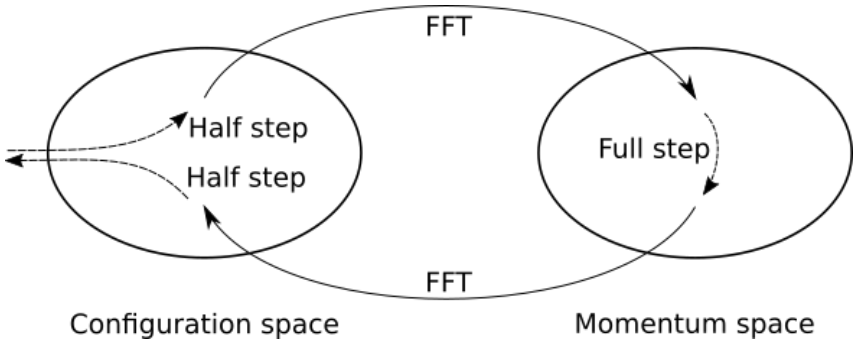

Figure D.1: A diagramtic illustration of the prodcedure followed when completing time evolution with the split-step method. Here 'FFT' refers to applying fast Fourier transforms and the 'steps' refer to application of the exponentiated operations from eq. (D.1.2).

The split-step method is unconditionally stable,[50] but requires that the Hamiltonian can be split into separate kinetic and potential terms.

D.2 Lanczos method

The short iterative Lanczos method instead works by recasting the initial wave function $|\Psi\rangle := \left|\vec{r}, \Psi(t)\right\rangle$ in terms of an orthonormal finite Krylov basis $\left\{|\phi_i\rangle\right\}$ of size n where[50,53,54]

$$\text{span}\left\{|\phi_i\rangle\right\} = \text{span}\left\{|\phi_1\rangle, \hat{H}|\phi_1\rangle, \hat{H}^2|\phi_1\rangle, ..., \hat{H}^n|\phi_1\rangle\right\}, \tag{D.2.1}$$

for $|\phi_1\rangle := \frac{|\Psi\rangle}{\sqrt{\langle\Psi|\Psi\rangle}}$. Since this basis is generated using the Hamiltonian, it should be able to describe the immediate time evolution of $|\Psi\rangle$.[49,50] To construct $\left\{|\phi_i\rangle\right\}$ we take[49,52,54]

$$|\psi_2\rangle := \hat{H}|\phi_1\rangle \tag{D.2.2}$$
$$\langle\phi_2|\psi_2\rangle|\phi_2\rangle = |\psi_2\rangle - \langle\phi_1|\psi_2\rangle|\phi_1\rangle \tag{D.2.3}$$
$$|\psi_3\rangle := \hat{H}|\phi_2\rangle \tag{D.2.4}$$
$$\langle\phi_3|\psi_3\rangle|\phi_3\rangle = |\psi_3\rangle - \langle\phi_2|\psi_3\rangle|\phi_2\rangle - \langle\phi_1|\psi_3\rangle|\phi_1\rangle. \tag{D.2.5}$$

Now note that by Hermiticity

$$\langle\phi_1|\psi_3\rangle = \langle\phi_1|\hat{H}|\phi_2\rangle = \langle\phi_2|\hat{H}|\phi_1\rangle = \langle\phi_2|\psi_2\rangle. \tag{D.2.6}$$

Using eq. (D.2.3), it is clear that $\langle\phi_3|\psi_2\rangle = 0$, thus when constructing $|\phi_4\rangle$ we see

$$|\psi_4\rangle := \hat{H}|\phi_3\rangle \tag{D.2.7}$$
$$\langle\phi_4|\psi_4\rangle|\phi_4\rangle = |\psi_4\rangle - \langle\phi_3|\psi_4\rangle|\phi_3\rangle - \langle\phi_2|\psi_4\rangle|\phi_2\rangle - \langle\phi_1|\psi_4\rangle|\phi_1\rangle, \tag{D.2.8}$$

but from the Hermiticity shown in eq. (D.2.6) $\langle\phi_1|\psi_4\rangle = \langle\phi_3|\psi_2\rangle = 0$. This follows in general and we find that for $k \in \mathbb{Z} \cap [3, n]$[49,52,54]

$$\begin{aligned} \beta_k |\phi_k\rangle &= \hat{H} |\phi_{k-1}\rangle - \alpha_{k-1} |\phi_{k-1}\rangle - \beta_{k-2} |\phi_{k-2}\rangle \\ \text{where} \quad \alpha_k &:= \langle\phi_k|\hat{H}|\phi_k\rangle \\ \text{and} \quad \beta_k &:= \langle\phi_k|\hat{H}|\phi_{k+1}\rangle \end{aligned} \tag{D.2.9}$$

This gives the tridiagonal representation of $\hat{H}$ in the Krylov basis $\{|\phi_i\rangle\}$ of size n as

$$H_n = \begin{pmatrix} \alpha_1 & \beta_1 & & & & \\ \beta_1 & \alpha_2 & \beta_2 & & & \\ & \beta_2 & \ddots & \ddots & & \\ & & \ddots & \alpha_{n-2} & \beta_{n-2} & \\ & & & \beta_{n-2} & \alpha_{n-1} & \beta_{n-1} \\ & & & & \beta_{n-1} & \alpha_n \end{pmatrix}. \tag{D.2.10}$$

By determining the eigenvalues λ_k and eigenfunctions $|\lambda_k\rangle$ of H_n we can then evolve $|\Psi\rangle$ in time to obtain[49,54]

$$\big|\Psi(\vec{r}, t + \Delta t)\big\rangle = \sum_k \exp\left(-\frac{i}{\hbar}\lambda_k \Delta t\right) \big\langle\lambda_k\big|\Psi(\vec{r}, t)\big\rangle\, |\lambda_k\rangle\,. \tag{D.2.11}$$

Within the short iterative Lanczos method, the same Krylov basis is used to propagate the wave function a small number of time steps without loss of accuracy.[49,50,54] Although the tridiagonalisation of the Hamiltonian and subsequent determination of the eigenfunctions and eigenvalues is not very computationally efficient, the fact that this does not need to be completed for every timestep compensates for this. For more complex simulations, such as simulating tweezer merging in more than one dimension, this may make the short iterative Lanczos method more efficient than the split-step method.

An animation roughly demonstrating how this Lanczos method can be used to give the time evolution of a Gaussian wave packet in a harmonic potential can be found at

https://sjmwhite.com/durham/msci-project/anim/1/harmonic/lanczos.mp4

Appendix E
Animations

In this chapter we include URL links to a number of animations created during our simulations. These help to provide additional insight into the processes we observe and aid with the visualisation of the results which we present in our main report.

These animations are predominately presented using the simulation units we describe in section 2.2.

E.1 Linear transport in a harmonic potential

In this section, we include links to animations showing the motion of the Cs wave function from the wave function's frame when it is transported $82\,a_h = 2.5\,\mu m$ in a harmonic potential using a linear trajectory.

E.1.1 Integer harmonic oscillation period

In these animations, the transport time is $t_f = 2.0\,T_h$ (twice the oscillation period in the potential). As predicted in eq. (3.1.3), we thus see a faithful transport with minimal excitations at the end of the motion.

Transport in frame of the wave function:

https://sjmwhite.com/durham/msci-project/anim/1/harmonic/lin/2-0_wf.mp4

Transport in the frame of the 938 nm optical tweezer:

https://sjmwhite.com/durham/msci-project/anim/1/harmonic/lin/2-0_twzr.mp4

E.1.2 Half-integer harmonic oscillation period

In these animations, the transport time is $t_f = 2.5\,T_h$ (two and a half times the oscillation period in the potential). As predicted in section 3.1.1, we see that the wave function becomes motionally excited at the end of the motion.

Transport in frame of the wave function:

https://sjmwhite.com/durham/msci-project/anim/1/harmonic/lin/2-5_wf.mp4

Transport in the frame of the 938 nm optical tweezer:

https://sjmwhite.com/durham/msci-project/anim/1/harmonic/lin/2-5_twzr.mp4

E.2 Linear transport in 938 nm tweezer

The animations in this section are equivalent to those given in section E.1, except the transports are now completed using the 938 nm optical tweezer potential. These are examples of the simulations used to obtain the data presented in fig. 3.2.

E.2.1 Integer harmonic oscillation period

Animations for $t_f = 2.0\,T_h$.

Transport in frame of the wave function:

https://sjmwhite.com/durham/msci-project/anim/1/gaussian/lin/2-0_wf.mp4

Transport in the frame of the 938 nm optical tweezer:

https://sjmwhite.com/durham/msci-project/anim/1/gaussian/lin/2-0_twzr.mp4

E.2.2 Half-integer harmonic oscillation period

Animations for $t_f = 2.5\,\mathrm{T_h}$.

Transport in frame of the wave function:

https://sjmwhite.com/durham/msci-project/anim/1/gaussian/lin/2-5_wf.mp4

Transport in the frame of the 938 nm optical tweezer:

https://sjmwhite.com/durham/msci-project/anim/1/gaussian/lin/2-5_twzr.mp4

E.3 Transport with minimum-jerk trajectory in 938 nm tweezer

These animations show the transport of the Cs atom in the 938 nm optical tweezer using the minimum-jerk trajectory.

E.3.1 Initial probability maximum

These animations show that the initial ground state occupation probability maximum at $t_f = 1.89\,\mathrm{T_h}$ results since the transport time is just the right length such that the Cs atom completes precisely one oscillation during the transport. The subsequent probability maxima result from similar conditions being met.

Transport in frame of the wave function:

https://sjmwhite.com/durham/msci-project/anim/1/gaussian/mj/1-89_wf.mp4

Transport in the frame of the 938 nm optical tweezer:

https://sjmwhite.com/durham/msci-project/anim/1/gaussian/mj/1-89_twzr.mp4

E.4 Transport with Lewis-Riesenfeld trajectories in 938 nm tweezer

Here we transport the single Cs atom in the 938 nm tweezer using the Lewis-Riesenfeld trajectories we described in section 3.3. Here, the trajectory is tailored such that the atom essentially completes a single oscillation in the tweezer potential irrespective of the transport duration.

E.4.1 Long transport times

Here we present animations for transport using the Lewis-Riesenfeld trajectories where the harmonic approximation of the $938\,\mathrm{T_h}$ hold to a good approximation.

$t_f = 2.0\,\mathrm{T_h}$

Transport in frame of the wave function:

https://sjmwhite.com/durham/msci-project/anim/1/gaussian/lr/2-0_wf.mp4

Transport in the frame of the 938 nm optical tweezer:

https://sjmwhite.com/durham/msci-project/anim/1/gaussian/lr/2-0_twzr.mp4

$t_f = 3.3\,\mathrm{T_h}$

Transport in frame of the wave function:

https://sjmwhite.com/durham/msci-project/anim/1/gaussian/lr/3-3_wf.mp4

Transport in the frame of the 938 nm optical tweezer:

https://sjmwhite.com/durham/msci-project/anim/1/gaussian/lr/3-3_twzr.mp4

E.4.2 Short transport times

The anharmonicity of the Gaussian potential means that the Lewis-Riesenfeld trajectories become less well matched to the transport motion for short transport times where $t_f \lesssim 1.8\,\mathrm{T_h}$. This can be seen in the sub-optimal transport shown in the following animations for $t_f = 1.1\,\mathrm{T_h}$.

Transport in frame of the wave function:

https://sjmwhite.com/durham/msci-project/anim/1/gaussian/lr/1-1_wf.mp4

Transport in the frame of the 938 nm optical tweezer:

https://sjmwhite.com/durham/msci-project/anim/1/gaussian/lr/1-1_twzr.mp4

E.5 Tweezer merging

These animations demonstrate the tweezer merging process where the 938 nm tweezer is moved with a (compensated) linear trajectory for a merge taking $24.8\,\mu\mathrm{s} = 2.0\,\mathrm{T_h}$.

E.5.1 Effective potentials

These animations demonstrate how the effective potentials for each atom change during the merging process. We show the Gaussian potentials resultant from each tweezer, the effective potential and (in the case of the Cs potential) the harmonic approximation to the potential that we use. The potential depths are plotted using the initial Cs trap frequency as ω.

Cs effective potential:

https://sjmwhite.com/durham/msci-project/anim/2/lin-c/2-0_cs_eff.mp4

From this animation, it is clear that the harmonic approximation around the Cs potential minimum becomes less accurate towards the end of the merging process as the effective potential becomes shallower and asymmetric. The deviation between the potential

minimum and tweezer locations may also make the determination of the harmonic trap frequency using eq. (4.1.5) less accurate here as explained in section 4.1.2.

Rb effective potential:

https://sjmwhite.com/durham/msci-project/anim/2/lin-c/2-0_rb_eff.mp4

Please note that the initial offset of the effective potential is an artefact resulting from the method we have used to position the effective potential in this animation. It has no origin within our numerical simulations or any physical basis.

E.5.2 Atomic behaviour

These animations show how the atomic wave functions behave during the merging process. This animations are taken from the frames of the 938 nm and 814 nm optical tweezers, thus clearly show the deviations of the potential minima from the tweezer locations during the merging process.

The units of energy given utilise the effective harmonic trap frequency at each timestep in the simulation ω_{instant} which is calculated using eq. (4.1.5).

Cs wave function motion:

https://sjmwhite.com/durham/msci-project/anim/2/lin-c/2-0_cs_twzr.mp4

Rb wave function motion:

https://sjmwhite.com/durham/msci-project/anim/2/lin-c/2-0_rb_twzr.mp4

Appendix F
Tabulated results

In this chapter we include tables illustrating the transport/merge times at which particular ground state occupation probabilities were exceeded in our simulations for a number of different trajectories.

F.1 One tweezer transport

The results in this section relate to transporting a single Cs atom a distance of $d = 82\,a_h = 2.5\,\mu m$ in the isolated 938 nm optical tweezer. This is fully discussed in chapter 3.

Trajectory	Transport time required to exceed given value of P_{Cs} (µs)						
	30 %	50 %	70 %	90 %	99 %	99.5 %	99.9 %
Linear	205.2	>250	>250	>250	>250	>250	>250
Minimum-jerk	33.0	33.7	43.9	55.0	81.1	92.8	132.0
Lewis-Riesenfeld	16.5	17.0	17.7	18.9	20.7	21.2	22.0

Table F.1: The minimum transport times t_f required to achieve different ground state occupation probabilities P_{Cs} for the transport of a Cs atom in an isolated 938 nm tweezer. For all values of t_f greater than those give, P_{Cs} does not fall below the specified value in the table header.

F.2 Tweezer merging

The tabulated results in this section relate to completing the merging process between the 938 nm tweezer initially containing a single Cs atom and the 814 nm tweezer which initially contains a Rb atom.

We first present results corresponding to the figures we show in chapter 4 within table F.2.

Trajectory	Merge time required to exceed given probability (µs)								
	P_{Cs}			P_{Rb}			$P_{combined}$		
	50 %	90 %	99 %	50 %	90 %	99 %	50 %	90 %	99 %
Minimum-jerk	91.3	117.1	147.1	57.1	73.9	99.5	92.0	117.4	150.1
Rigid L-R	87.8	115.9	146.1	55.8	73.2	99.0	88.6	116.4	149.4
Non-rigid L-R	71.5	102.5	144.4	56.6	74.9	98.2	73.9	104.5	150.4
Full L-R	15	31.5	54.8	33.0	54.6	114.4	33.7	56.3	115.6

Table F.2: The minimum times required to merge the 938 nm and 814 nm optical tweezers and obtain the given ground state occupation probabilities (GSOPs). Here, P_{Cs} is the GSOP for the Cs atom, P_{Rb} is the GSOP for Rb, $P_{combined} = P_{Cs} \times P_{Rb}$ and 'L-R' stands for Lewis-Riesenfeld. The 'Full L-R' trajectory is the one described in section 4.3 where the 938 nm tweezer power is adjusted during the merging process.

The results in this table correspond to the figures that we have included in appendix G. We have not included any results for merges completed using a linear trajectory since

it takes a merge time of longer than 370 µs before a 90 % Cs ground state occupation probability is reached (see fig. G.5).

Trajectory	Merge time required to exceed given probability (µs)								
	P_{Cs}			P_{Rb}			P_{combined}		
	50 %	90 %	99 %	50 %	90 %	99 %	50 %	90 %	99 %
Minimum-jerk	208.9	293.3	>370	37.2	51.1	71.2	209.1	294.0	>370
Rigid L-R	201.7	287.3	>370	36.0	50.9	71.7	201.7	288.3	>370
Non-rigid L-R	165.0	243.1	355.8	37.7	56.3	78.2	165.0	243.9	>370
Full L-R (small Δt)	14.6	33.0	54.3	34.0	57.0	>62	35.0	60	>62

Table F.3: The minimum times required to merge the 938 nm and 814 nm optical tweezers and obtain the given ground state occupation probabilities (GSOPs). Here, P_{Cs} is the GSOP for the Cs atom, P_{Rb} is the GSOP for Rb, $P_{\mathrm{combined}} = P_{\mathrm{Cs}} \times P_{\mathrm{Rb}}$ and 'L-R' stands for Lewis-Riesenfeld. All of the trajectories except the 'Full L-R' one were completed without trajectory compensation using eq. (4.1.2). The 'Full L-R' trajectory was completed under identical simulation conditions to those for the trajectory described in section 4.3, except that the timestep was decreased to $\Delta t = 1 \times 10^{-4}\,\mathrm{T_h} = 1.24\,\mathrm{ns}$.

Appendix G
Supplementary merging results

In this appendix we have included additional results which further support our discussions in the main report text. All of the result we include relate to merging the 938 nm and 814 nm optical tweezers in a similar fashion to that described in chapter 4.

G.1 Uncompensated trajectory results

The results in this section were collected when simulating the tweezer merging process without using eq. (4.1.2) to move the potential minima using our desired trajectories. Thus we move the optical tweezers using the specified trajectory.

G.1.1 Minimum-jerk trajectory

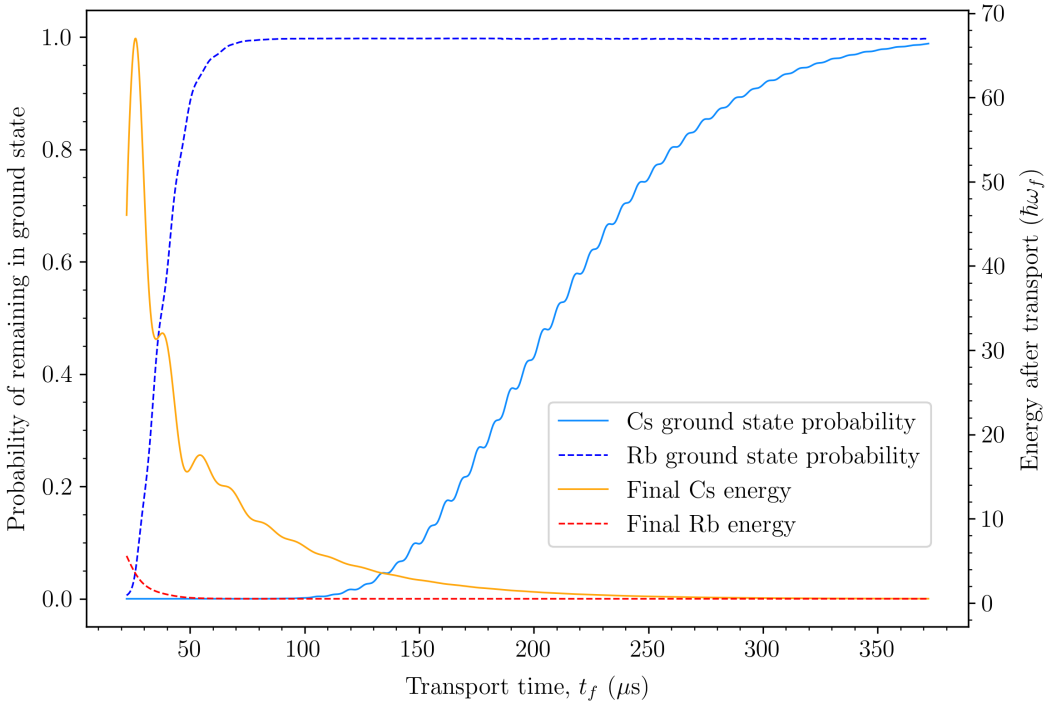

Figure G.1: Results from uncompensated tweezer merging using the minimum-jerk trajectory.

G.1.2 Rigid Lewis-Riesenfeld trajectories

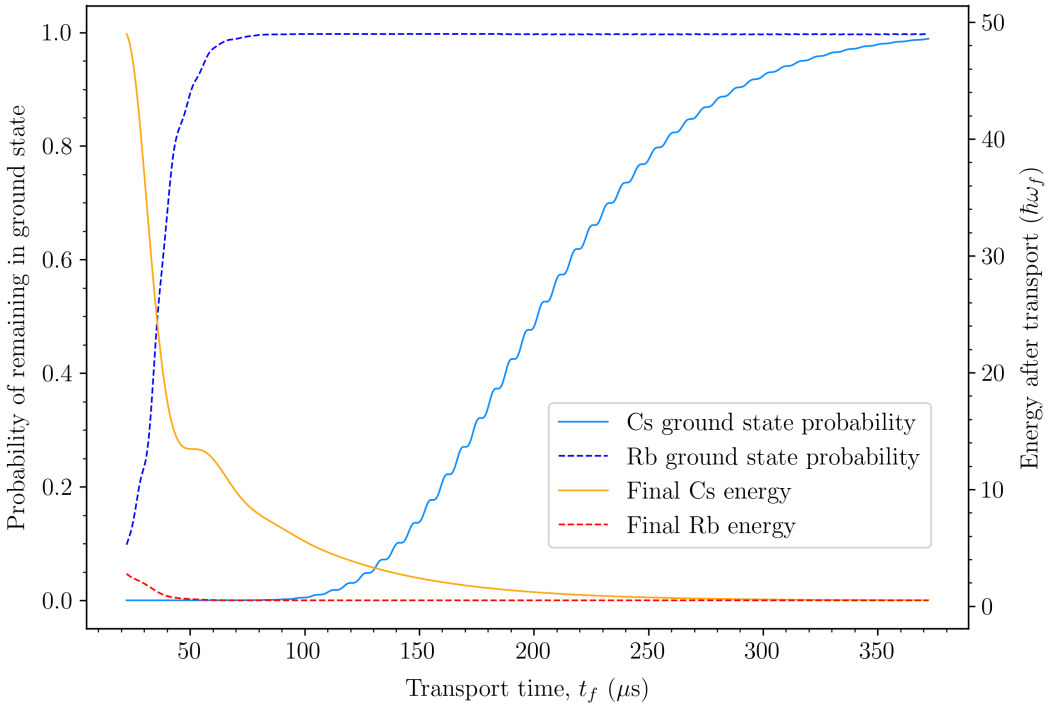

Figure G.2: Results from uncompensated tweezer merging using the rigid Lewis-Riesenfeld trajectories.

G.1.3 Non-rigid Lewis-Riesenfeld trajectories

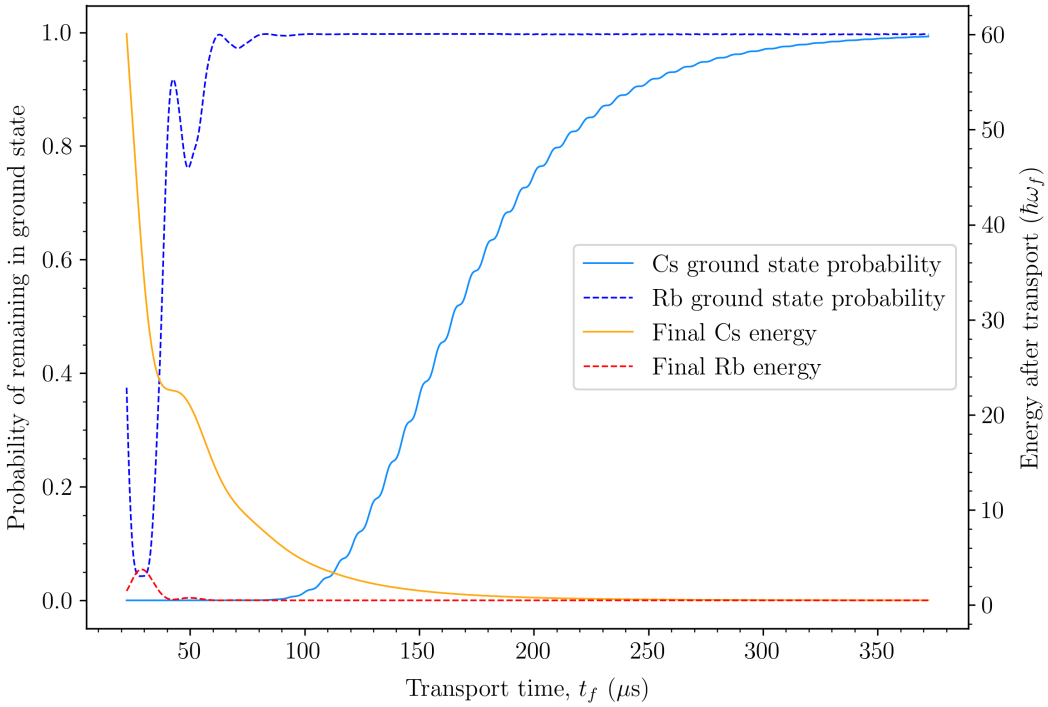

Figure G.3: Results from uncompensated tweezer merging using the non-rigid Lewis-Riesenfeld trajectories.

G.2 Frequency control with smaller timestep

These results where obtained using the same conditions as those used for fig. 4.4, but with a timestep one hundred times smaller of $\Delta t = 1 \times 10^{-4}\,\mathrm{T_h} = 1.24\,\mathrm{ns}$. These results demonstrate near identical behaviour for the ground state occupation probabilities as fig. 4.4 even though the variations in the trap frequency are much smaller.

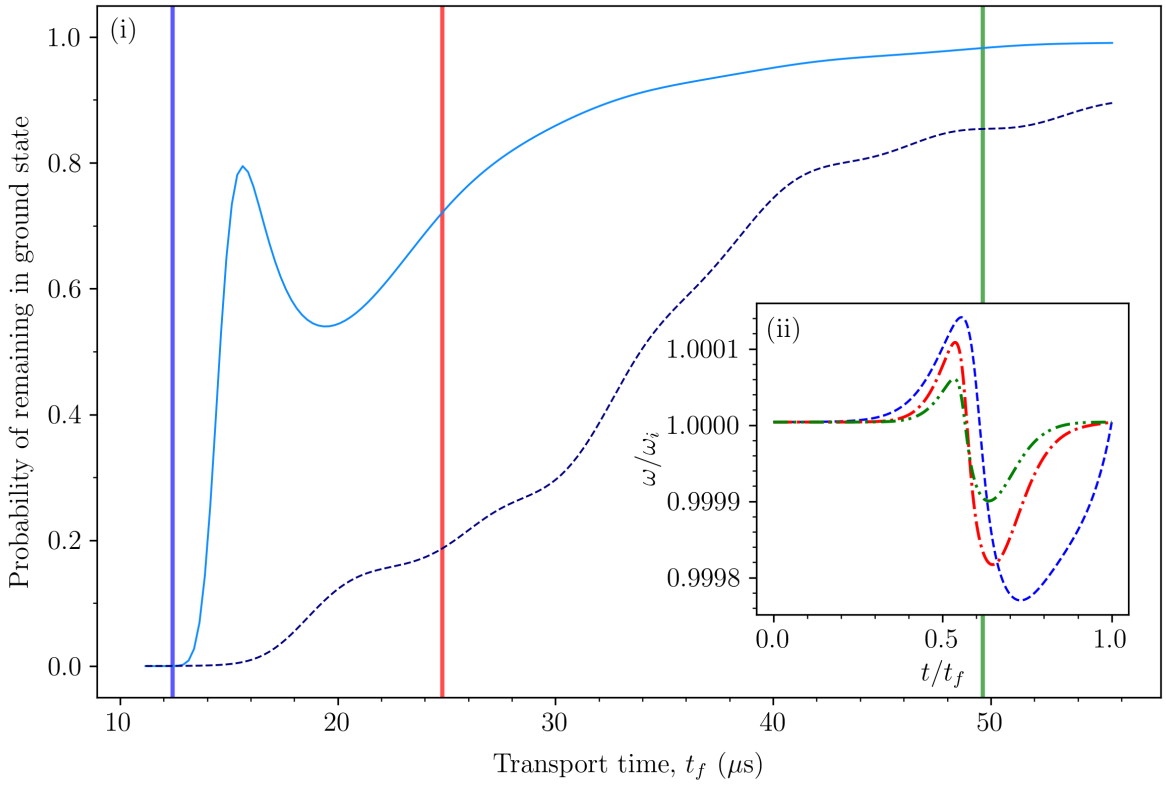

Figure G.4: (i) Results obtained by attempting to keep the trap frequency constant during the tweezer merge with a timestep $\Delta t = 1 \times 10^{-4}\,\mathrm{T_h} = 1.24\,\mathrm{ns}$. The solid pale blue line shows the probability of ground state occupation for the Cs atom, while the dashed navy line shows this for the Rb atom. (ii) How the Cs harmonic trap frequency changes during the merge where ω_i is the initial trap frequency.

G.3 Linear trajectory

Figure G.5 shows the results for a linear merge between the two tweezers using a tweezer trajectory calculated using eq. (4.1.2). We have not included these results in the main report text since this merging requires very long merging times in order to obtain reliably high Cs ground state occupation probabilities.

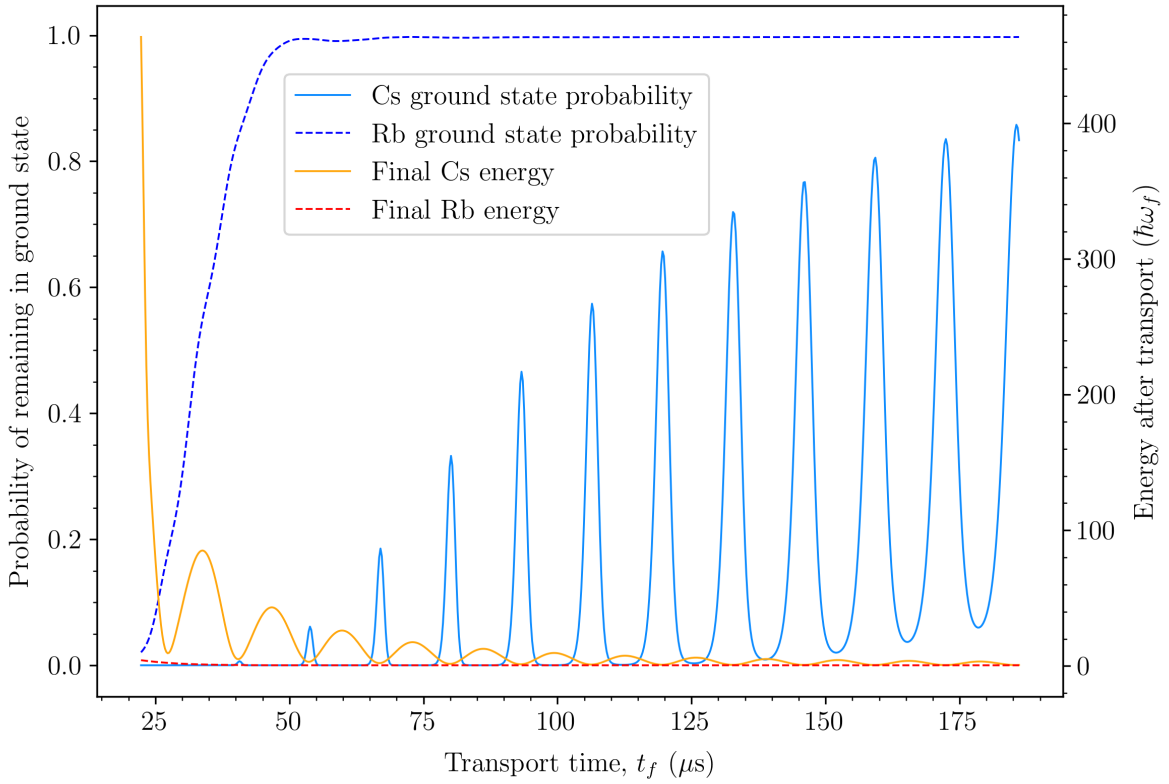

Figure G.5: Results from merging the two optical tweezers using a linear trajectory with the 938 nm tweezer position compensated using eq. (4.1.2).

Appendix H
Simulation code

The Julia code written to implement our simulations is publicly available on GitHub. This is split into the three different standalone packages described in the sections below. The code which interfaces with these packages to construct our simulations is not yet publicly available.

H.1 QuantumSimulation

The QuantumSimulation package contain code implementing the split step and short iterative Lanczos numerical simulation methods. Additionally, it contains definitions for special data types used for quantum mechanical objects and recipes for plotting the information associated with them. We have also included functions in this package for completing the trajectory translation described in section 4.1.1 and constructing the potentials used.

https://github.com/sw104/QuantumSimulation.jl

H.2 UnitfulAtomicHarmonic

The UnitfulAtomicHarmonic package extends the (third party) Unitful.jl package to allow easy implementation of the simulation units described in section 2.2 and facilitate easy conversions between unit systems.

https://github.com/sw104/UnitfulAtomicHarmonic.jl

H.3 HarmonicTrapTrajectories

Our HarmonicTrapTrajectories package is a small package which helps with the implementation of the trajectories we used in this project.

https://github.com/sw104/HarmonicTrapTrajectories.jl